PHYSICAL REVIEW D **91,** 095004 (2015)

Discrimination of dark matter models in future experiments

Tomohiro Abe,[1] Ryuichiro Kitano,[1,2] and Ryosuke Sato[1]

[1]*Institute of Particle and Nuclear Studies, High Energy Accelerator Research Organization (KEK) Tsukuba 305-0801, Japan*

[2]*The Graduate University for Advanced Studies (Sokendai) Tsukuba 305-0801, Japan*

(Received 12 November 2014; published 5 May 2015)

Phenomenological aspects of simple dark matter models are studied. We discuss ways to discriminate the dark matter models in future experiments. We find that the measurements of the branching fraction of the Higgs boson into two photons, the electric dipole moment of the electron, and the direct-detection experiments are quite useful in discriminating particle models of dark matter. We also discuss the prospects of finding new particles in the dark sector at the LHC/ILC.

DOI: 10.1103/PhysRevD.91.095004 PACS numbers: 95.35.+d, 12.60.-i, 12.60.Fr

I. INTRODUCTION

Dark matter (DM) was first proposed by Oort [1] and Zwicky [2] to explain the motion of stars in our Galaxy or galaxies in clusters. Eighty years have passed since then, and various evidence (e.g., galaxy rotation curves, gravitational lensing, the precision measurement of the cosmic microwave background, etc.) support the existence of dark matter. However, we still do not know what dark matter is. Various candidates have been proposed. The most promising one is a weakly interacting massive particle (WIMP) [3]. Since there is no candidate for such a particle in the standard model (SM), this scenario requires an extension of the SM.

The recent discovery of the Higgs boson and the measurements of its properties strongly support the origin of the Higgs boson as a component of the $\mathrm{SU}(2)_L$ doublet Higgs field. The precise measurement of its properties—aimed at understanding the nature of the Higgs field—is one of the most important tasks in particle physics. It is quite possible that the DM particle couples to the SM through the Higgs field so that the DM abundance is explained as a thermal relic. In that case, the Higgs boson as well as other SM particles carry information on DM. In the literature, various particle models have been proposed and their phenomenology has been studied (see, for example, Refs. [4–19]).

In this paper, we survey simple extensions of the SM to account for dark matter using the WIMP scenario, and summarize the current situations and future prospects of observing signatures of each model. We list six renormalizable models to realize the WIMP scenario as examples, and compare the model predictions to see if we can distinguish models by various measurements. We review and summarize the status of each model thoroughly, and also show new results such as the predictions for the electron electric dipole moment (EDM) in the fermionic dark matter models. We examine which observables are important in each model, and discuss the differences.

This paper is organized as follows. In Sec. II, we introduce the dark matter models that we will discuss in this paper. In Secs. III and IV, we briefly review the phenomenology of each of the models, especially focusing on the spin-independent cross section, the Higgs invisible decay, the Higgs diphoton signal, and the electron EDM. We require that each model explains the energy density of the dark matter abundance $\Omega_{\mathrm{DM}}h^2 = 0.1196 \pm 0.0031$ (reported by the Planck Collaboration [20]). In Sec. V, we discuss how to discriminate models in future experiments. Section VI is devoted to a conclusion and discussions.

II. DARK MATTER MODELS

In this section, we list the dark matter models that we will discuss in this paper. We add new field(s) to the SM and introduce Z_2 parity which guarantees the stability of the dark matter. Under this Z_2 parity, all of the SM fields are even and the new fields are odd. We take the minimal renormalizable Lagrangian which includes a candidate for dark matter. We summarize the models in Table I.

A. Singlet scalar dark matter (model S1)

In this model, an additional $\mathrm{SU}(2)_L$ singlet real scalar s with hypercharge $Y = 0$ is introduced [4–6]. The mass and interaction terms for s are given by

TABLE I. List of dark matter models. Numbers in a parentheses attached to the field represent the $\mathrm{SU}(2)_L \times \mathrm{U}(1)_Y$ representation. For the Lagrangian of each model, see each section.

Model	Z_2 odd field(s)	Parameters
S1 (Sec. II A)	$s(1_0)$	m_s, λ_{sH}
S2 (Sec. II B)	$H_2(2_{1/2})$	m_{A^0}, m_{S^0}, m_{H^+}, λ_A, λ_2
F12 (Sec. II D)	$\psi_S(1_0), \psi_D(2_{-1/2}), \chi_D(2_{1/2})$	m_S, m_D, λ, λ', θ
F23 (Sec. II E)	$\psi_D(2_{-1/2}), \chi_D(2_{1/2}), \psi_T(3_0)$	m_D, m_T, λ, λ', θ

$$\mathcal{L}_{\rm S1} = -\frac{m_1^2}{2}s^2 - \frac{\lambda_{sH}}{2}s^2|H|^2 - \frac{\lambda_s}{4!}s^4. \quad (1)$$

The self-interaction term s^4 does not affect the following discussion. The mass eigenvalue of s is given by $m_s^2 = m_1^2 + \lambda_{sH}v^2/2$, where $v \simeq 246$ GeV is the vacuum expectation value of the Higgs field.

B. Doublet scalar dark matter (model S2)

In this model, an additional $\mathrm{SU}(2)_L$ doublet scalar H_2 with hypercharge $Y = 1/2$ is introduced [8,21]. The mass and interaction terms for H_2 are given by

$$\mathcal{L}_{\rm S2} = -m_2^2|H_2|^2 - \lambda_1|H|^4 - \lambda_2|H_2|^4 - \lambda_3|H|^2|H_2|^2 - \lambda_4|H^\dagger H_2|^2 - \left[\frac{\lambda_5}{2}(H_2^\dagger H)^2 + \text{H.c.}\right]. \quad (2)$$

In general, λ_5 is a complex parameter however, its phase can be taken away by a redefinition of H_2. In the following, we take λ_5 as real and positive. H_2 is decomposed as

$$H_2 = \begin{pmatrix} H^+ \\ (S^0 + iA^0)/\sqrt{2} \end{pmatrix}, \quad (3)$$

where H^+ is a charged scalar field and S^0 and A^0 are neutral real scalar fields. In the unitary gauge, the interaction terms between additional scalar particles and the Higgs boson are given by

$$\begin{aligned}\mathcal{L}_{\rm S2} \ni & -\lambda_3|H|^2|H_2|^2 - \lambda_4|H^\dagger H_2|^2 - \frac{\lambda_5}{2}[(H_2^\dagger H)^2 + \text{H.c.}] \\ &= -\lambda_3|H^+|^2\left(\frac{v+h}{\sqrt{2}}\right)^2 - \frac{\lambda_S}{2}s^2\left(\frac{v+h}{\sqrt{2}}\right)^2 \\ &\quad - \frac{\lambda_A}{2}a^2\left(\frac{v+h}{\sqrt{2}}\right)^2, \end{aligned} \quad (4)$$

where $\lambda_S \equiv \lambda_3 + \lambda_4 + \lambda_5$ and $\lambda_A \equiv \lambda_3 + \lambda_4 - \lambda_5$ are effective couplings to the Higgs boson. Their mass eigenvalues are given by

$$m_{H^+}^2 = m_2^2 + \frac{\lambda_3}{2}v^2, \qquad m_{S^0}^2 = m_2^2 + \frac{\lambda_S}{2}v^2, \qquad m_{A^0}^2 = m_2^2 + \frac{\lambda_A}{2}v^2. \quad (5)$$

$\lambda_A < \lambda_S$ and $m_{A^0} < m_{S^0}$ are satisfied because we take λ_5 as real and positive. Furthermore, if $\lambda_4 < \lambda_5$, A^0 becomes lighter than H^+. In this situation, A^0 becomes the candidate for dark matter. The conditions for the scalar potential to be bounded from below are given by [8]

$$\min[\lambda_A, \lambda_S, \lambda_3] = \lambda_A > -2\sqrt{\lambda_1\lambda_2}, \qquad \lambda_2 > 0.$$

C. Triplet scalar/fermion model (models S3 and F3)

If we add an SU(2) triplet scalar (t)/fermion (χ) with $Y = 0$, we can construct simple dark matter models[1] [12,22]. Here, we call them models S3 and F3, respectively. Model F3 is an effective theory of the wino dark matter model [23,24]. The Lagrangians of these models are given by

$$\mathcal{L}_{\rm S3} = \mathcal{L}_{\rm SM} + \frac{1}{2}(\partial t)^2 - \frac{m_3^2}{2}t^2 - \frac{\lambda_{tH}}{2}t^2|H|^2, \quad (6)$$

$$\mathcal{L}_{\rm F3} = \mathcal{L}_{\rm SM} + i\psi_T \not{\partial}\psi_T - \left(\frac{M_T}{2}\psi_T\psi_T + \text{H.c.}\right). \quad (7)$$

In model S3, we can write the dark matter self-interaction term t^4. However, this self-interaction term does not affect our discussion, and thus we neglect it.

Model S3 has a neutral scalar t^0 and a charged scalar t^+, and model F3 has a neutral Majorana fermion ψ_T^0 and a charged Dirac fermion ψ_T^+. In both of these models, the masses of the neutral particle and the charged particle are degenerated. The mass splitting between them is generated by a one-loop radiative correction [22]. In model S3, for $m_{t^0}, m_{t^\pm} \gg m_W, m_Z$,

$$m_{t^+} - m_{t^0} \simeq \frac{\alpha_2}{2}(m_W - c_W^2 m_Z) \simeq 166 \text{ MeV}, \quad (8)$$

and, in model F3, for $m_{\chi^0}, m_{\chi^\pm} \gg m_W, m_Z$,

$$m_{\psi_T^+} - m_{\psi_T^0} \simeq \frac{\alpha_2}{2}(m_W - c_W^2 m_Z) \simeq 166 \text{ MeV}. \quad (9)$$

Hence, in both of the models, charged particles becomes slightly heavier than neutral ones. In such a situation, dark matter coannihilation becomes important to obtain the correct amount of thermal relic abundance, and thus the mass of the dark matter tends to be large. We can get the correct relic abundance for $m_{t^0} \sim 2.5$ TeV in model S3, and $m_{\psi_T^0} \sim 2.7$ TeV in model F3 [13]. It is difficult to discuss these models in the context of near-future collider experiments, and thus we do not discuss them in detail.

D. Singlet-doublet fermion dark matter (model F12)

Here we discuss the singlet-doublet mixed fermion dark matter model [14–18]. We introduce three left-handed Weyl fermions: an SM singlet fermion (ψ_S), and two $\mathrm{SU}(2)_L$ doublet fermions with $Y = -1/2$ (ψ_D) and $Y = 1/2$ (χ_D). If we only introduce the singlet fermion ψ_S, a dimension-five interaction $(1/\Lambda)\psi_S\psi_S|H|^2$ is required to annihilate

[1]One might think that model F2 [namely, the SU(2) doublet Dirac fermion with $Y = 1/2$] is also a simple possibility. However, dark matter with nonzero hypercharge is severely constrained by the direct-detection experiments [22].

into the SM particles [25]. In this paper, we focus on the renormalizable model of dark matter and do not consider this possibility. In model F12, thanks to the $SU(2)_L$ doublet fermions ψ_D and χ_D, we can construct a renormalizable Lagrangian. This matter content is vector-like, and this model is free from gauge anomalies. The renormalizable interaction terms for the dark matter sector are given by

$$\mathcal{L}_{\rm F12} = -\frac{1}{2} m_S \psi_S \psi_S - m_D \psi_D \chi_D + y \tilde{H}^\dagger \psi_S \psi_D + y' H^\dagger \psi_S \chi_D + \text{H.c.}, \tag{10}$$

where $\tilde{H} = \epsilon H^*$ and ϵ is a totally antisymmetric tensor. We have four complex parameters in the dark matter sector. Among them, three phases can be removed by a redefinition of ψ_S, ψ_D, and χ_D. In this paper, we take a basis in which m_S, m_D, and y are real and positive. Finally, we have the following five physical free parameters in this model:

$$m_S, m_D, y, |y'|, \theta \equiv \arg(y'). \tag{11}$$

In this model, we have one charged Dirac fermion and three neutral Majorana fermions. The mass of the charged fermion is m_D. The mass eigenstates of the neutral fermions are a mixture of ψ_S, ψ_D^0, and χ_D^0. Their mass matrix is given by

$$\mathcal{L}_{\rm mass} = -\frac{1}{2} \begin{pmatrix} \psi_S & \psi_D^0 & \chi_D^0 \end{pmatrix} \begin{pmatrix} m_S & yv/\sqrt{2} & -y'v/\sqrt{2} \\ yv/\sqrt{2} & 0 & -m_D \\ -y'v/\sqrt{2} & -m_D & 0 \end{pmatrix} \begin{pmatrix} \psi_S \\ \psi_D^0 \\ \chi_D^0 \end{pmatrix}. \tag{12}$$

Each mass eigenstate f can be written as a linear combination of ψ_S, ψ_D^0, and χ_D^0:

$$\begin{pmatrix} \psi_S \\ \psi_D^0 \\ \chi_D^0 \end{pmatrix} = \begin{pmatrix} U_{11} & U_{12} & U_{13} \\ U_{21} & U_{22} & U_{23} \\ U_{31} & U_{32} & U_{33} \end{pmatrix} \begin{pmatrix} f_1^0 \\ f_2^0 \\ f_3^0 \end{pmatrix}, \tag{13}$$

where U is the unitary matrix. We define the following four-component Dirac and Majorana spinors:

$$\Psi^+ \equiv \begin{pmatrix} \chi_D^+ \\ \psi_D^{-\dagger} \end{pmatrix}, \qquad \Psi_i^0 \equiv \begin{pmatrix} f_i^0 \\ f_i^{0\dagger} \end{pmatrix}. \tag{14}$$

The relevant interaction terms for the calculation of the parameters S and T and the EDM are given by

$$\mathcal{L}_{\rm int} = g \bar{\Psi}^+ \gamma^\mu (\mathcal{C}_{L,i} P_L + \mathcal{C}_{R,i} P_R) \Psi_i^0 W_\mu^+ + g \bar{\Psi}_i^0 \gamma^\mu (\mathcal{C}_{L,i}^* P_L + \mathcal{C}_{R,i}^* P_R) \Psi^+ W_\mu^- + \frac{g}{2 c_W} \bar{\Psi}_i^0 \gamma^\mu (\mathcal{N}_{L,ij} P_L + \mathcal{N}_{R,ij} P_R) \Psi_j^0 Z_\mu + \frac{g}{c_W} \left(\frac{1}{2} - s_W^2 \right) \bar{\Psi}^+ \gamma^\mu \Psi^+ Z_\mu, \tag{15}$$

where $\mathcal{C}_{L,i}$, $\mathcal{C}_{R,i}$, $\mathcal{N}_{L,ij}$, and $\mathcal{N}_{R,ij}$ are determined by the mixing matrix U:

$$\mathcal{C}_{L,i} = \frac{1}{\sqrt{2}} U_{3i}, \qquad \mathcal{C}_{R,i} = -\frac{1}{\sqrt{2}} U_{2i}^*, \qquad \mathcal{N}_{L,ij} = -\mathcal{N}_{R,ji} = \frac{1}{2} (U_{3i}^* U_{3j} - U_{2i}^* U_{2j}). \tag{16}$$

Let us comment on the symmetry of this model. In the case when $\theta = 0$ or π, we can take all of the parameters in the dark matter sector as real by using a redefinition of ψ_S, ψ_D, and χ_D, i.e., CP is conserved in the dark matter sector. On the other hand, in the cases when $\theta \neq 0, \pi$, the dark matter sector does violate CP symmetry. The dark matter sector gives contributions to the EDMs of the SM particles. If $y = |y'|$, we have charge conjugation symmetry as $\psi_D \leftrightarrow \chi_D$. In this case, the dark matter-dark matter-Z boson coupling vanishes. Furthermore, ψ_D and χ_D form an $SU(2)_R$ doublet and the dark matter sector has a custodial symmetry in this case, and the contribution of Z_2-odd particles to the T parameter vanishes at the one-loop level.

E. Doublet-triplet fermion dark matter (model F23)

Here, we discuss the doublet-triplet mixed fermion dark matter model [19]. We introduce three left-handed Weyl

fermions, an $SU(2)_L$ doublet fermion with $Y=-1/2$ (ψ_D) and $Y=1/2$ (χ_D), and an $SU(2)_L$ triplet fermion (ψ_T) with $Y=0$. This matter content is vector-like, and thus it is free from gauge anomalies. The renormalizable interaction terms in the dark matter sector are given by

$$\mathcal{L}_{\rm F23} = -\frac{1}{2}m_S\psi_T\psi_T - m_D\psi_D\chi_D + y\tilde{H}^\dagger\psi_T\psi_D + y' H^\dagger\psi_T\chi_D + \text{H.c.} \tag{17}$$

We have four complex parameters in the dark matter sector. Among them, three phases can be removed by a redefinition of ψ_D, χ_D, and ψ_T. In this paper, we take a basis in which m_D, m_T, and y are real and positive. In this basis, we have the following five physical free parameters:

$$m_D, m_T, y, |y'|, \theta \equiv \arg(y'). \tag{18}$$

In this model, there are two charged Dirac fermions and three neutral Majorana fermions. The mass matrices of the fermions are given by

$$\mathcal{L}_{\rm mass} = -\frac{1}{2}\begin{pmatrix}\psi_D^0 & \chi_D^0 & \psi_T^0\end{pmatrix}\begin{pmatrix}0 & -m_D & yv/\sqrt{2}\\ -m_D & 0 & -y'v/\sqrt{2}\\ yv/\sqrt{2} & -y'v/\sqrt{2} & m_T\end{pmatrix}\begin{pmatrix}\psi_D^0\\ \chi_D^0\\ \psi_T^0\end{pmatrix} - \begin{pmatrix}\chi_D^+ & \psi_T^+\end{pmatrix}\begin{pmatrix}m_D & y'v\\ yv & m_T\end{pmatrix}\begin{pmatrix}\psi_D^-\\ \psi_T^-\end{pmatrix}. \tag{19}$$

Each mass eigenstates f can be written as a linear combination of ψ_D, χ_D, and ψ_T:

$$\begin{pmatrix}\psi_D^0\\ \chi_D^0\\ \psi_T^0\end{pmatrix} = \begin{pmatrix}U_{11}^0 & U_{12}^0 & U_{13}^0\\ U_{21}^0 & U_{22}^0 & U_{23}^0\\ U_{31}^0 & U_{32}^0 & U_{33}^0\end{pmatrix}\begin{pmatrix}f_1^0\\ f_2^0\\ f_3^0\end{pmatrix}, \tag{20}$$

$$\begin{pmatrix}\chi_D^+\\ \psi_T^+\end{pmatrix} = \begin{pmatrix}U_{11}^+ & U_{12}^+\\ U_{21}^+ & U_{22}^+\end{pmatrix}\begin{pmatrix}f_1^+\\ f_2^+\end{pmatrix}, \qquad \begin{pmatrix}\psi_D^-\\ \psi_T^-\end{pmatrix} = \begin{pmatrix}U_{11}^- & U_{12}^-\\ U_{21}^- & U_{22}^-\end{pmatrix}\begin{pmatrix}f_1^-\\ f_2^-\end{pmatrix}, \tag{21}$$

where U^0, U^+, and U^- are unitary matrices. We define the following four-component Dirac and Majorana spinors:

$$\Psi_i^+ \equiv \begin{pmatrix}f_i^+\\ f_i^{-\dagger}\end{pmatrix}, \qquad \Psi_i^0 \equiv \begin{pmatrix}f_i^0\\ f_i^{0\dagger}\end{pmatrix}. \tag{22}$$

The situation is similar to model F12 regarding the phases and custodial symmetry. In the case when $\theta = 0$ and π, we can take all the parameters in the dark matter sector as real by using redefinitions of ψ_D, χ_D and ψ_T. For $y = |y'|$, we have charge conjugation symmetry as $\psi_D \leftrightarrow \chi_D$, which results in a vanishing dark matter-dark matter-Z boson coupling. Due to the custodial symmetry at this point, the contribution of Z_2-odd particles to the T parameter vanishes at the one-loop level.

III. PHENOMENOLOGY OF EACH OF THE MODELS

In this section, we discuss phenomenological aspects of the dark matter models introduced in the previous section. We will thoroughly study the models and summarize the results in order to compare them in Sec. V. There are various studies on each of these models in the literature, and some of the results presented here overlap with those works. We list references of these works in the subsection of each model. The analysis of model F12 includes the effect of the CP-violating phase, which was not fully explored in previous studies, and we discuss model F12 in Sec. IV. In the following analysis we use FEYNRULES [26] and MICROMEGAs [27] to calculate the relic abundance of dark matter and the Higgs invisible decay width. We take the Higgs boson mass as 125 GeV [28,29] throughout this paper.

A. Model S1

In model S1, there are only two parameters which are relevant to dark matter physics, i.e., the dark matter mass $m_{\rm DM}$ and the dark matter-Higgs coupling λ_{sH}. By imposing the condition that the relic abundance explains the DM of the Universe, λ_{sH} is fixed as a function of $m_{\rm DM}$, and thus $m_{\rm DM}$ is the only free parameter. In the following we compute the direct-detection cross section as a function of the dark matter mass. If the dark matter mass is smaller than half of the Higgs boson mass, the Higgs boson can decay into two dark matter particles [4,30,31]. This contributes to the branching fraction of the invisible decay

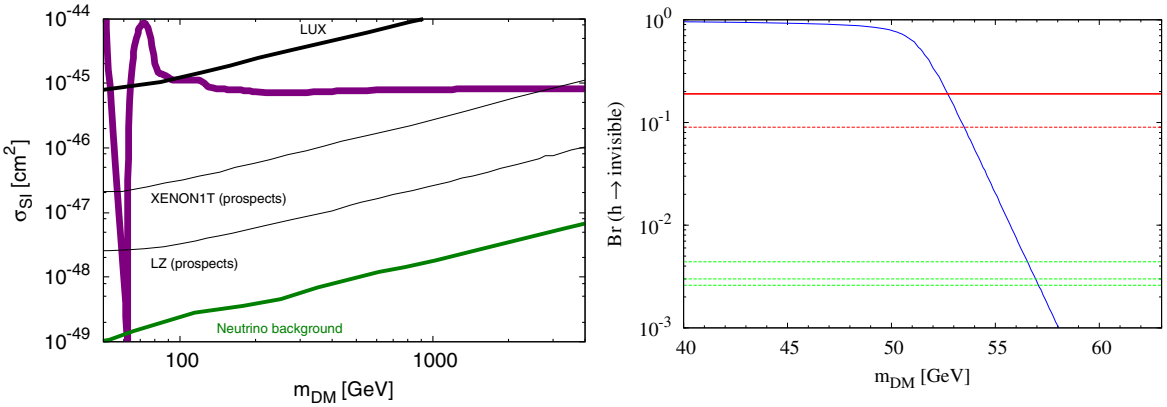

FIG. 1 (color online). Present status of the scalar dark matter S1 model. Left: The wide mass range of the dark matter mass is shown. The purple line is the model prediction. The black bold solid line is the current bound from the LUX experiment. The green line shows the discovery limit which is caused by atmospheric and astrophysical neutrinos. We also plot future prospects of the XENON1T and LZ experiments. Right: The branching fraction of the Higgs invisible decay in the S1 model. The red solid line is the current bound. The red dashed line is the future prospect at the LHC at 300 fb^{-1}. The three green dashed lines are the future prospects at the ILC (250 GeV with 250 fb^{-1}, 500 GeV with 500 fb^{-1}, and 1 TeV with 1 ab^{-1}, respectively).

of the Higgs boson; we also discuss this here. For comprehensive studies of this model, see, e.g., Refs. [6,7,31–35].

1. Relic abundance and direct detection

In this model, the dark matter can scatter with nucleons via the interaction term with the Higgs boson [4,6]. This coupling also determines the annihilation cross section of the dark matter. Thus, direct-detection experiments give an important constraint on the model. Here, we show the constraint on the spin-independent cross section (σ_{SI}) from the LUX experiment [36]. The left panel of Fig. 1 shows σ_{SI} as a function of the dark matter mass m_{DM}, where the correct dark matter abundance is imposed. The mass region with 53 GeV $\lesssim m_{\mathrm{DM}} \lesssim$ 64 GeV and 100 GeV $\lesssim m_{\mathrm{DM}}$ are allowed by the constraint from the LUX experiment. We also show the future prospects of the XENON1T and LZ experiments [37], and the dark matter discovery limit which is caused by atmospheric and astrophysical neutrinos [38].

2. Higgs invisible decay

If the mass of the dark matter is smaller than half of the Higgs boson, the Higgs boson can decay into a pair of dark matter particles [4,30]. The right panel of Fig. 1 shows the branching fraction of the Higgs invisible decay as a function of the dark matter mass m_{DM}, while also requiring the correct dark matter abundance. The current bound on the branching fraction of the invisible decay of the Higgs boson in model S1 is $\mathrm{Br}(h \to \mathrm{invisible}) < 0.19$ [11]. This is shown with the red solid line in the figure. Thus the lower bound on the dark matter mass is 53 GeV, which coincides with that from the LUX experiment. The LHC can reach $\mathrm{Br} = 0.09$ with 300 fb^{-1} [39], and the ILC can reach $\mathrm{Br} = 0.0026$ with $\sqrt{s} = 1$ TeV and 1 ab^{-1} [39]. These lines are shown in the figure.

In Fig. 2, we focus on the light DM mass region. The information on the branching fraction of the Higgs invisible decay is also shown. We see that XENON1T will cover the ILC reach. Therefore, in this model, if XENON1T finds the DM signal in the lighter mass range $m_{\mathrm{DM}} < m_h/2$, the ILC should also find the Higgs invisible decay.

B. Model S2

In model S2, the dark matter couplings to the SM particles are determined by $\mathrm{SU}(2)_L \times U(1)_Y$ gauge couplings and λ_A, which is defined in Sec. II B. After fixing the size of λ_A by the relic abundance, we discuss the spin-independent cross section in the direct-detection

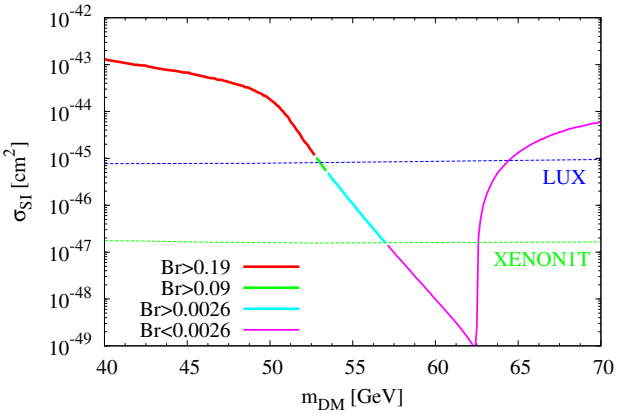

FIG. 2 (color online). The dark matter mass around half of the Higgs mass is shown. The line shows the parameter regions which can realize $\Omega_{\mathrm{DM}}h^2 = 0.12029$ [20]. The red, green, cyan, and purple solid lines are $0.19 < \mathrm{Br}(h \to \mathrm{invisible})$, $0.09 < \mathrm{Br}(h \to \mathrm{invisible}) < 0.19$, $0.0026 < \mathrm{Br}(h \to \mathrm{invisible}) < 0.09$, and $\mathrm{Br}(h \to \mathrm{invisible}) < 0.0026$, respectively. The green and blue dashed lines are the current bounds from the LUX experiment and the future prospect of the XENON1T experiment.

experiments. We find that there are two dark matter mass regions: $m_{\rm DM} \lesssim 72$ GeV and $m_{\rm DM} \gtrsim 600$ GeV. We also discuss the mass bound on m_{H^+} and m_{S^0} from LEP2 and electroweak precision bounds. Then we focus on the light dark matter mass region and discuss the contribution of the dark matter to the branching fraction of the invisible decay, and the diphoton channel of the Higgs boson. We find that the branching fraction of the invisible decay has similar behavior as the S1 model, and the signal strength of $h \to \gamma\gamma$ is ∼10% smaller than that in the SM. For comprehensive studies of this model, see, e.g., Refs. [10,40–44].

1. Relic abundance and direct detection

In the region of light dark matter in model S2, the annihilation of dark matter is similar to that in model S1 [45]. Thus, the direct-detection experiments give an important constraint on the model. We have four free parameters: $m_{\rm DM}(= m_{A^0})$, m_{S^0}, m_{H^+} and λ_A. The value of λ_A can be fixed by requiring the correct amount of relic abundance. We have three remaining mass parameters. In Fig. 3, we show the spin-independent cross section $\sigma_{\rm SI}$ as a function of dark matter mass $m_{\rm DM}$ in the dark matter S2 model, while also requiring the correct dark matter abundance.

The parameter space that gives the correct amount of dark matter is split into two regions: the light mass region $m_{\rm DM} \lesssim 72$ GeV and the heavy mass region $m_{\rm DM} \gtrsim 500$ GeV. In the light mass region, the Higgs boson s-channel exchange diagrams give the dominant contribution to the dark matter annihilation cross section. If $m_{S^0} - m_{A^0}$ and $m_{H^+} - m_{A^0}$ are large enough, the S2 dark matter behaves similarly to the S1 dark matter at the tree-level calculation, as we can see from Fig. 3. However, for $m_{\rm DM} \sim m_h/2$ (i.e., small λ_A), we note that one-loop radiative corrections give a significant modification to the spin-independent cross section for model S2 dark matter [46], because it is charged under the electroweak gauge group. In the figure, the tree-level cross section is shown. For $m_{\rm DM} > m_W$, the $A^0A^0 \to W^+W^-$ channel opens and the annihilation cross section becomes large. Therefore, unlike model S1, the abundance of S2 dark matter becomes too small to explain $\Omega_{\rm DM}h^2$ for $m_{\rm DM} \gtrsim m_W$. For $m_{\rm DM} \gtrsim 500$ GeV, a viable region reappears. The relic abundance in the heavy mass region is very sensitive to mass splittings between dark matter and the heavier particles S^0 and $H^\pm$.

2. Direct search

We have determined two parameters ($m_{\rm DM}$ and λ_A) by imposing the correct relic density. The remaining parameters are m_{H^+} and m_{S^0}.

At e^+e^- colliders, H^+ can be produced via the process $e^+e^- \to (Z/\gamma)^* \to H^+H^-$. The LEP2 experiment gives a lower bound on the mass of $H^\pm$ of 70–90 GeV [47]. Also, neutral scalar bosons can be produced via the process $e^+e^- \to Z^* \to A^0S^0$ [48] (see Fig. 4). For dark matter lighter than the W boson, we find that a viable parameter region exists for $m_{S^0} - m_{A^0} \gtrsim 40$ GeV, with a small window around $m_{S^0} - m_{A^0} \simeq 8$ GeV.

For 65 GeV $< m_{\rm DM} <$ 70 GeV, we see that the exclusion from the spin-independent cross section is sensitive to the charged Higgs mass. In this region, we need to take the $A^0A^0 \to WW^*$ process into account in the relic density. The diagram exchanging the charged Higgs in the t channel contributes to this process, and it is destructive with the same process when the Higgs boson is in the s channel. Therefore, the heavier charged Higgs requires the smaller Higgs coupling to the DM to reproduce the correct relic abundance, and thus the spin-independent cross section is also smaller when the charged Higgs is heavier. Note that the spin-independent cross section in this region is on the edge of the exclusion limit, as can be seen from Fig. 3.

At the LHC, model S2 can be probed by searching for dilepton and missing energy signals [49] and trilepton and missing energy signals [50]. For 40 GeV $\lesssim m_{\rm DM} \lesssim$ 72 GeV,

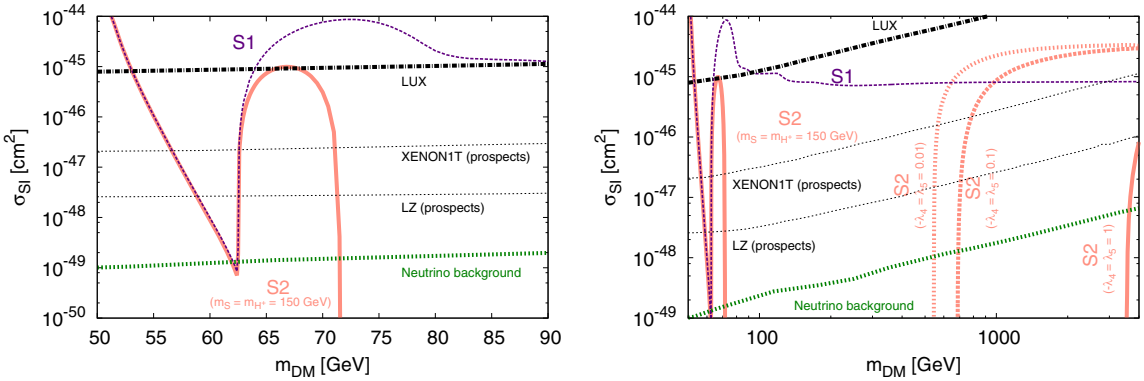

FIG. 3 (color online). Present status of model S2. Each line shows the parameter regions that can realize $\Omega_{\rm DM}h^2 = 0.12029$ [20]. The purple dotted line shows model S1, while the pink lines shows model S2. In the left panel, we take $m_{S^0} = m_{H^+} = 150$ GeV. In the right panel, we take $m_{S^0} = m_{H^+} = 150$ GeV for the leftmost pink line. For the other lines, we take $-\lambda_4 = \lambda_5$ as 0.01, 0.1, and 1 from left to right. The black chain line shows the constraint from the LUX experiment. The green dotted lines show the discovery limit caused by atmospheric and astrophysical neutrinos [38]. We also plot the future prospects of XENON1T and LZ [37].

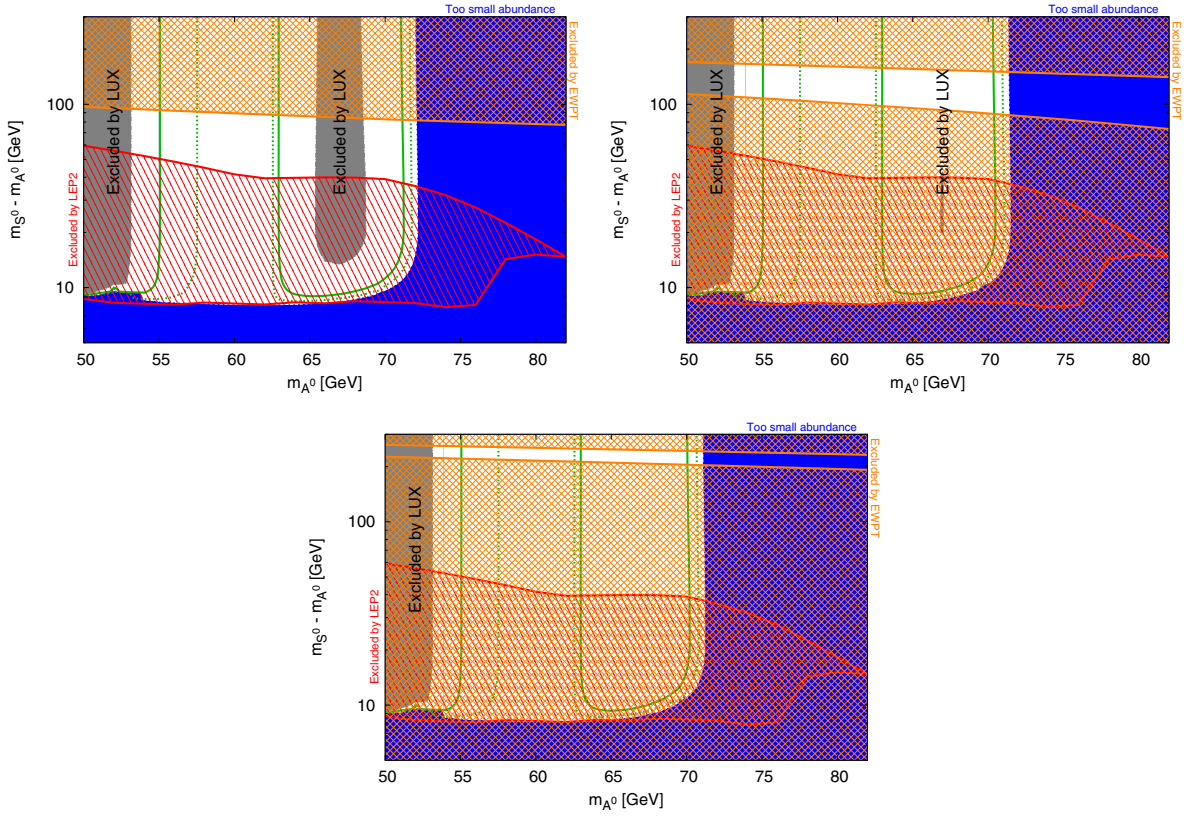

FIG. 4 (color online). The LEP2 constraint in the $m_{A^0} - (m_{S^0} - m_{A^0})$ plane. In the blue regions, the thermal relic abundance becomes too small. In this figure, we take $m_{H^+} = 120$ GeV (upper left), $m_{H^+} = 200$ GeV (upper right), and $m_{H^+} = 300$ GeV (lower). The red meshed regions are excluded by the LEP2 experiment [48]. The gray regions are excluded by the LUX experiment. The yellow regions are excluded by the S and T parameters. The green solid and dotted lines show $\sigma_{\rm SI} = 10^{-46}$ and 10^{-47} cm^2, respectively.

this search has a sensitivity in the parameter region with $m_{H^+,S^0} \simeq 100$–180 GeV.

3. S and T parameters

As discussed in Refs. [8,51,52], inert doublet Higgs fields give a contribution to electroweak precision tests (EWPT). In this section, we discuss electroweak precision measurements. The gauge boson two-point functions are given as

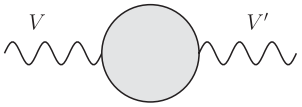

$$= i\Pi_{VV'}(p^2)g^{\mu\nu} + i\Delta_{VV'}p^\mu p^\nu. \tag{23}$$

By using this, the Peskin-Takeuchi parameters [53] are defined as

$$S = \frac{4s^2c^2}{\alpha}\left(\frac{\Pi_{ZZ}(m_Z^2) - \Pi_{ZZ}(0)}{m_Z^2} - \frac{c^2 - s^2}{sc}\frac{\Pi_{Z\gamma}(m_Z^2)}{m_Z^2} - \frac{\Pi_{\gamma\gamma}(m_Z^2)}{m_Z^2}\right), \tag{24}$$

$$T = \frac{1}{\alpha}\left(\frac{\Pi_{WW}(0)}{m_W^2} - \frac{\Pi_{ZZ}(0)}{m_Z^2}\right). \tag{25}$$

The contributions to the $\Pi_{VV'}$'s from the dark matter sector are given by

$$\Pi_{WW} = \frac{g^2}{16\pi^2}\tilde{B}_{22}(m_{H^+}, m_s) + \frac{g^2}{16\pi^2}\tilde{B}_{22}(m_{H^+}, m_a), \tag{26}$$

$$\Pi_{ZZ} = \frac{1}{16\pi^2}\frac{g^2}{c^2}(\tilde{B}_{22}(m_s, m_a) + (c^2 - s^2)^2\tilde{B}_{22}(m_{H^+}, m_{H^+})), \tag{27}$$

$$\Pi_{Z\gamma} = \frac{eg}{c}\frac{c^2 - s^2}{8\pi^2}\tilde{B}_{22}(m_{H^+}, m_{H^+}), \tag{28}$$

$$\Pi_{\gamma\gamma} = \frac{e^2}{4\pi^2}\tilde{B}_{22}(m_{H^+}, m_{H^+}). \tag{29}$$

The definitions of $\tilde{B}_{22}$ are given in the Appendix.[2] We show the numerical result of the constraint for $m_{\rm DM} = 55$ GeV in

[2]We have checked that our formulas are consistent with Ref. [8] in the limit of $m_{S^0}, m_{A^0}, m_{H^+} \gg m_Z$.

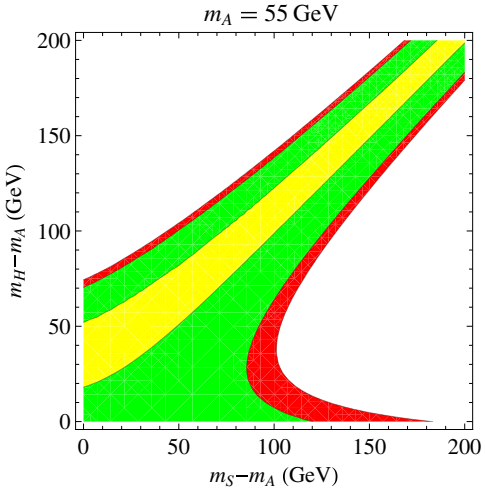

FIG. 5 (color online). The constraint from the S and T parameters for $m_{\rm DM} = 55$ GeV. The yellow, green, and red regions are allowed at 31.7%, 90%, and 95% C.L., respectively.

Fig. 5. We find that large mass differences between the dark matter and other Z_2-odd particles are disfavored except for the $m_{S^0} \sim m_{H^+}$ case. Note that when $m_{H^+} = m_{S^0}$, the custodial symmetry appears in the Z_2-odd sector, and thus the T parameter becomes zero at the one-loop level. The constraints are superimposed in Fig. 4.

4. Higgs invisible decay

The dark matter in model S2 has the very same coupling as that between dark matter and the Higgs in model S1, and the Higgs boson can decay invisibly if the mass of the dark matter is smaller than half of m_h [10,54]. Since there are viable parameter regions for $m_{A^0} < m_h/2$, we have a chance to observe the invisible decay of the Higgs boson. From the discussion on the LEP2 bound in Sec. III B 2 and the discussion on the electroweak precision bound in Sec. III B 3, it is natural to expect that $m_{S^0} \simeq m_{H^+} \gtrsim m_{\rm DM} + 40$ GeV. Then the S2 dark matter behaves similarly to the S1 dark matter, as can be seen from Fig. 3. We conclude that the branching fraction of the Higgs invisible decay as a function of dark matter mass in this model behaves the same as in the S1 model (shown in the right panel of Fig. 1).

5. Higgs diphoton decay signal

As discussed in Refs. [10,52,55], in model S2, loop diagrams including a charged scalar H^+ modify the branching fraction of the Higgs boson into two photons. Its decay width is given by

$$\Gamma(h \to 2\gamma) = \frac{G_F \alpha^2 m_h^3}{128\sqrt{2}\pi^3} \left| A_{\rm SM} + \frac{\lambda_3 v^2}{2m_{H^+}^2} A_0\left(\frac{m_h^2}{4m_{H^+}^2}\right) \right|^2, \quad (30)$$

where the second term in the absolute value is the contribution from H^+, and $A_{\rm SM}$ is the contribution from the SM particles, which is given by

$$A_{\rm SM} = A_1\left(\frac{m_h^2}{4m_W^2}\right) + \sum_f N_C Q_f^2 A_{1/2}^H\left(\frac{m_h^2}{4m_f^2}\right), \quad (31)$$

and its numerical value is $A_{\rm SM} \simeq -6.45$ for $m_h = 125$ GeV, $m_W = 80.4$ GeV, and $m_t = 173$ GeV. The definitions of the A functions are given in the Appendix. We can expect that the charged Higgs contribution does not decouple even if the charged Higgs mass is much larger than the electroweak scale as long as the mass difference between the dark matter and the charged Higgs mass is kept large. Because the mass differences among the Z_2-odd particles imply the sizable value of couplings of the Z_2-odd particles to the Higgs boson, (namely, sizable $\lambda_{3,4,5}$), the charged Higgs coupling to the Higgs boson remains even if its mass is quite large. We can confirm this expectation from Eq. (30). By using Eq. (5), λ_3 can be written using m_{H^+}, m_{A^0} and λ_A,

$$\frac{\lambda_3 v^2}{2m_{H^+}^2} = 1 - \frac{m_{A^0}^2}{m_{H^+}^2} + \frac{\lambda_A v^2}{2m_{H^+}^2}. \quad (32)$$

For $x \ll 1$, $A_0(x) \simeq 1/3 + 8x/45 + \cdots$. Thus, as long as we consider light dark matter A^0, even if the charged scalar is relatively heavy the charged Higgs contribution remains, and its asymptotic behavior is $\lambda_3 v^2/(2m_{H^+}^2)A_0 \to 1/3$ $(m_{H^+} \to \infty)$.

We show how the diphoton branching fraction is modified in Fig. 6. We find that the branching fraction to the diphoton channel deviates from the standard model by around 10%. The sensitivity to the diphoton signal strength is around 10% at the 14 TeV LHC with 300 fb^{-1}, and it reaches around 5% at the ILC [56]. We can conclude that model S2 can be probed at the ILC in the case of $m_{\rm DM} \lesssim 72$ GeV.

C. Model F23

Here, we discuss the phenomenology of model F23. This model has two parameter regions: a heavy dark matter

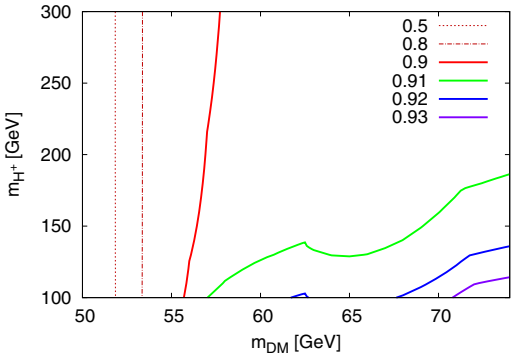

FIG. 6 (color online). Diphoton signal strength $\mu \equiv {\rm Br}(h \to 2\gamma)/{\rm Br}(h \to 2\gamma; {\rm SM})$ in the $m_{\rm DM}$–m_{H^+} plane. In this figure, we take $m_{S^0} = m_{\rm DM} + 100$ GeV.

region and a light dark matter region. In the heavy dark matter region, the mass difference between dark matter and heavier particles is small, and the coannihilation effect is significant. This situation is similar to wino or Higgsino dark matter, and in this case the dark matter mass becomes large and it is hard to see its effect in near-future experiments. In this paper, we only focus on the light dark matter region in which the coannihilation process is not important. Our analysis covers a wider parameter region than Ref. [19]. As we will see later, the measurement of the Higgs diphoton signal gives a severe constraint on the model.

1. Relic abundance and direct detection

We show the dark matter mass and the spin-independent cross section in Fig. 7. In this plot, we take the parameters of the model as $\lambda, \lambda' \in [0, 1.5]$, $m_D, m_T \in [0, 400]$ GeV, and $\theta \in [0, \pi]$. We calculate $\Omega_{\rm DM}h^2$, and extract the points which satisfy $0.1 \leq \Omega_{\rm DM}h^2 \leq 0.15$.

2. Higgs diphoton decay signal

Here, we show the Higgs diphoton signal strength. The interaction terms of the charged fermions χ are given by

$$\mathcal{L} = -y_{S,i}h\bar{\Psi}_i^+\Psi_i - iy_{P,i}h\bar{\Psi}_i^+\gamma^5\Psi_i^+, \tag{33}$$

where the couplings $y_{S,i}$ and $y_{P,i}$ are determined by λ, λ', U^+, and U^- in Eq. (21). The decay width of $h \to \gamma\gamma$ is given by

$$\Gamma(h \to \gamma\gamma) = \frac{G_F\alpha^2 m_h^3}{128\sqrt{2}\pi^3}\left(\left|A_{\rm SM} + \sum_i \frac{y_{S,i}v}{m_{\chi_i^\pm}} A_{1/2}^H\left(\frac{m_h^2}{4m_{\chi_i^\pm}^2}\right)\right|^2 + \left|\sum_i \frac{y_{P,i}v}{m_{\chi_i^\pm}} A_{1/2}^A\left(\frac{m_h^2}{4m_{\chi_i^\pm}^2}\right)\right|^2\right). \tag{34}$$

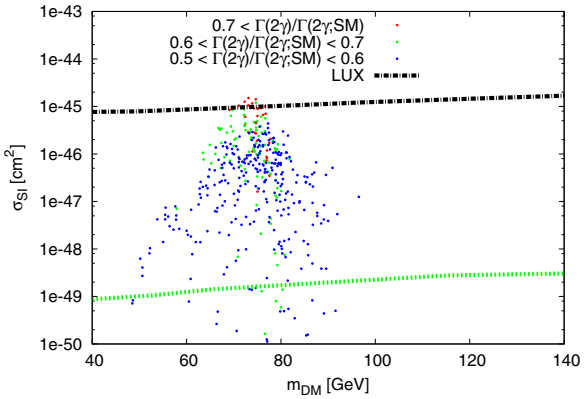

FIG. 7 (color online). Scatter plot of $m_{\rm DM}$-$\sigma_{\rm SI}$ for model F23. The black and green lines are the same as in Fig. 3. The red, green, and blue points satisfy $\mu(h \to 2\gamma) > 0.7$, $0.6 < \mu(h \to 2\gamma) < 0.7$, and $0.5 < \mu(h \to 2\gamma) < 0.6$, respectively.

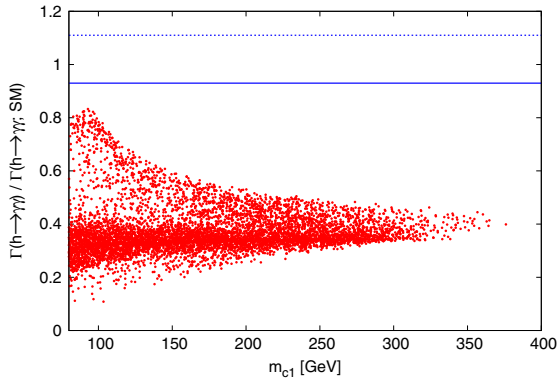

FIG. 8 (color online). Diphoton signal strength and mass of the lightest charged fermion in model F23. The region above the dotted (solid) blue line is consistent with the measurement of $h \to \gamma\gamma$ within 1σ (2σ) deviation.

We show how the diphoton branching fraction is modified in Fig. 8. In this plot, we take the parameters of the model as $\lambda, \lambda' \in [0, 1.5]$, $m_D, m_T \in [0, 400]$ GeV, and $\theta \in [0, \pi]$. Then, we calculate $\Omega_{\rm DM}h^2$ and extract the points which satisfy $0.1 \leq \Omega_{\rm DM}h^2 \leq 0.15$. We use the constraint on $m_{\chi_1^+}$ from the chargino search at the LEP experiment [57–60], $m_{\chi_1^+} \lesssim 93$ GeV. Applying this constraint, we can see from Fig. 8 that the diphoton signal strength deviates from the SM value, $\mu(h \to 2\gamma) < 0.85$. However, the diphoton signal strength measured at the LHC is $\mu(h \to 2\gamma) = 1.29 \pm 0.18$ (95% C.L.).[3] Therefore, the light dark matter region in this model is already excluded by LEP2 and the LHC. Hence, we do not investigate this model further in this paper.

IV. DETAILED ANALYSIS OF MODEL F12

One of the features of model F12 is a new CP-violating phase. Although its effect on EDMs was studied in Refs. [14,15], the abundance of dark matter and the cross section of the direct experiment were not fully explored in these references. In this section, we show the direct-detection cross section while taking into account the CP-violating phase.

A. Relic abundance and direct detection

We show the spin-independent direct-detection cross section for model F12 in Fig. 9. Here we consider the case that the model gives the correct dark matter abundance. Similar to models S1 and S2, direct detection gives a severe constraint on F12. In the case when the dark matter mass is around $m_h/2$ and $m_Z/2$, the spin-independent cross section becomes small. This is because (in these dark matter mass

[3]This value is obtained from the naive combination of $1.65^{+0.33}_{-0.28}$ from the ATLAS Collaboration [61] and $1.14 \pm 0.21({\rm stat})^{+0.09}_{-0.05}({\rm syst})^{+0.13}_{-0.09}({\rm theo})$ from the CMS Collaboration [62].

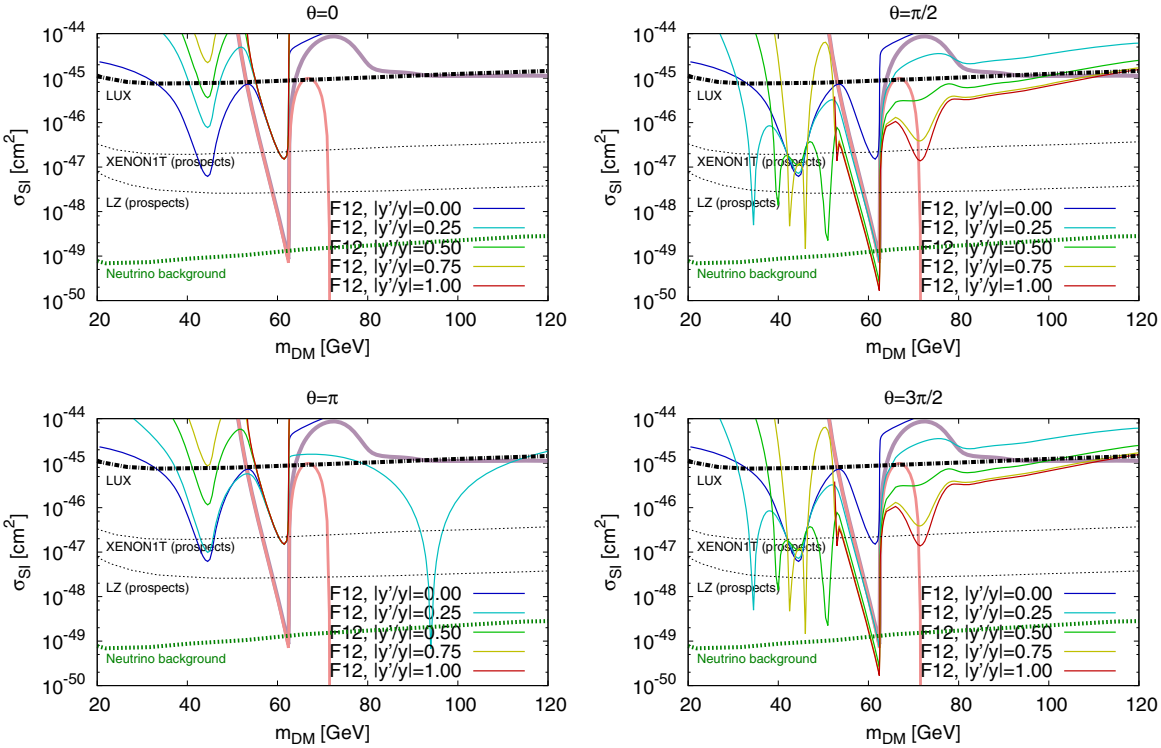

FIG. 9 (color online). The spin-independent cross section $\sigma_{\rm SI}$ of model F12. The blue, cyan, green, yellow, and red lines show $|y'/y| = 0, 0.25, 0.5, 0.75$, and 1, respectively. We take $m_D = 200$ GeV in these figures. For model F12, we take $\theta = 0$ (upper left), $\pi/2$ (upper right), π (lower left), and $3\pi/2$ (lower right). We also show $\sigma_{\rm SI}$ for model S1 (gray line) and model S2 with $m_{S^0} = m_{H^+} = m_{A^0} + 100$ GeV for reference.

regions) diagrams with a Higgs boson and a Z boson in the s channel give the dominant contribution to the annihilation cross section, which requires a small Higgs/Z-boson coupling to the DM.

In addition to this structure, the direct-detection cross section shows complicated structures when we turn on the phase of the Yukawa coupling, θ; see, for example, the 30 GeV $\lesssim m_{\rm DM} \lesssim$ 50 GeV region in the right panels in Fig. 9. We can understand this behavior as follows. The mass term and the interaction terms of the dark matter with the SM particles are written as

$$\mathcal{L} \ni -\frac{m_{\rm DM}}{2}\bar{\Psi}_1^0\Psi_1^0 + y_S h\bar{\Psi}_1^0\Psi_1^0 + iy_P h\bar{\Psi}_1^0\gamma^5\Psi_1^0 + ic_Z Z_\mu \bar{\Psi}_1^0\gamma^\mu\gamma^5\Psi_1^0. \tag{35}$$

Here, y_S, y_P, and c_Z are calculated from λ, λ', and the unitary matrix U which is defined in Eq. (13). Although all couplings (y_S, y_P, and c_Z) contribute to the annihilation cross section, only y_S contributes to the spin-independent cross section. This means that the spin-independent cross section becomes zero, and the correct relic abundance can be explained when $y_S = 0$, $y_P \neq 0$, and $c_Z \neq 0$. We found that $y_S = 0$ when the following condition is satisfied:

$$m_{\rm DM} = m_S = -m_D \sin 2\phi \cos\theta \quad (\theta = 0, \pi),$$
$$m_{\rm DM}^2 = \frac{m_S^2 m_D^2 \sin^2 2\phi \sin^2\theta}{m_S^2 + m_D^2 \sin^2 2\phi + 2m_S m_D \sin 2\phi \cos\theta} \quad (\theta \neq 0, \pi), \tag{36}$$

where $\tan\phi = |y/y'|$. Here we take $m_S > 0$ and $m_D > 0$ by using the freedom of the field redefinition, and thus $\theta = 0$ cannot satisfy this condition. When this condition is satisfied, we have a sizable annihilation cross section and a small spin-independent cross section. Such a parameter region is called a "blind spot" [18].

We also show the spin-dependent direct-detection cross section for model F12 given the correct dark matter abundance in Fig. 10. By comparing with Fig. 9, we find that the spin-dependent cross section gives a weaker bound than the spin-independent cross section in a wide region. An exception is the blind spots, where the dark matter couplings to the Z boson and to the Higgs boson with γ^5 are needed to reproduce the relic abundance; thus, the coupling to the Z boson can be large enough to make the spin-dependent cross section larger than the current bound. This is crucial in the blind spots for the $\theta = \pi$ case because the dark matter couplings to the Higgs boson completely vanish in this case, and thus the dark matter coupling to

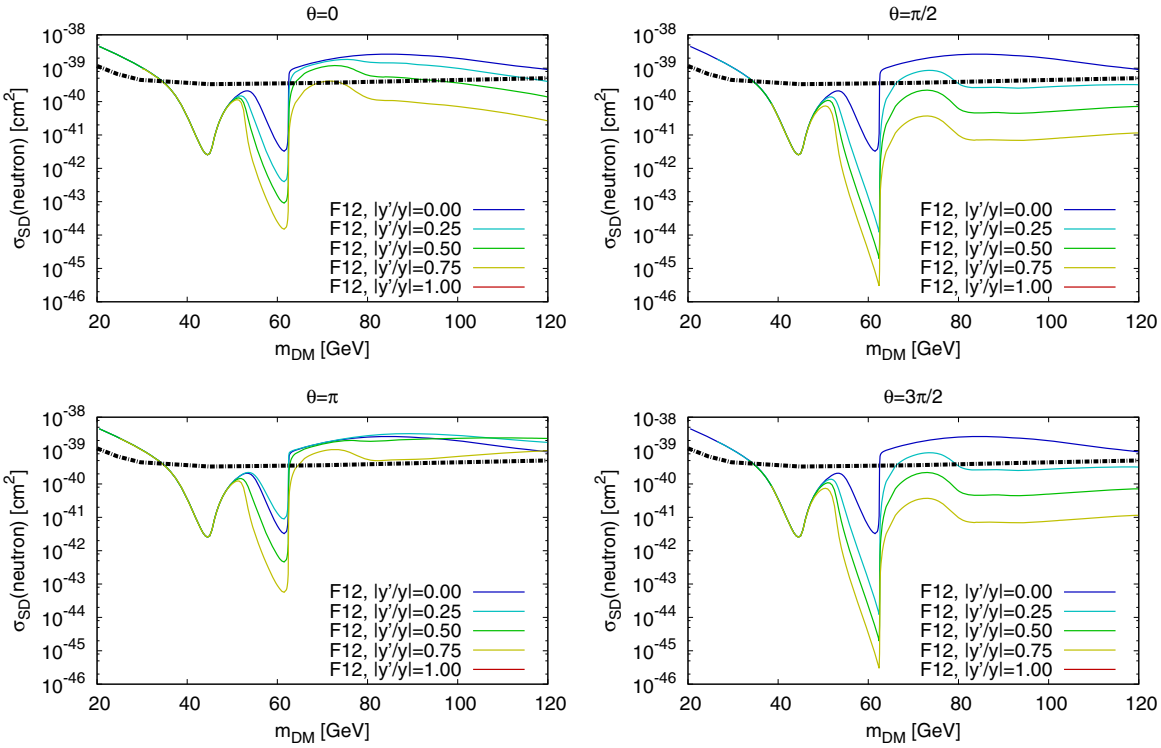

FIG. 10 (color online). The spin-dependent cross section $\sigma_{\rm SD}$ of model F12. The blue, cyan, green, yellow, and red lines show $|y'/y| = 0, 0.25, 0.5, 0.75$, and 1, respectively. We take $m_D = 200$ GeV in these figures. For model F12, we take $\theta = 0$ (upper left), $\pi/2$ (upper right), π (lower left), and $3\pi/2$ (lower right). We also show $\sigma_{\rm SI}$ for model S1 (gray line) and model S2 with $m_{S^0} = m_{H^+} = 150$ GeV for reference. The black lines show the constraint on the spin-dependent cross section of neutron-WIMP from XENON100 [63].

the Z boson must be sizable. We see this feature in the bottom-left panels in Figs. 9 and 10. In these panels, $\theta = \pi$ and there is a blind spot for $m_{\rm DM} \simeq 90$ GeV and $|y'/y| = 0.25$, and we find that this region is already excluded by the bound on the spin-dependent cross section.

A nonvanishing CP phase significantly enlarges the viable mass range of the dark matter by having y_S and y_P couplings simultaneously. We show in Fig. 11 the contour of the spin-independent cross section for various $|y'/y|$ ratios in the $m_{\rm DM}$–θ plane. As we will see later, such a CP phase induces the EDM of the electron, and thus a wide range of parameters can be covered by future EDM measurements.

B. Higgs invisible decay

If the mass of the dark matter is smaller than half of the Higgs boson mass, the Higgs invisible decay channel opens and we can use it as a probe of the dark matter sector. In Fig. 12, we show the branching fraction of the invisible decay of model F12. We calculate the partial decay width for the invisible decay $\Gamma_{\rm inv}$ using MICROMEGAs. The decay width of the Higgs boson in the SM is calculated as $\Gamma_{\rm SM} = 4.41 \times 10^{-3}$ GeV for $m_h = 125$ GeV using HDECAY [64]. The branching fraction of the invisible decay is given by $\Gamma_{\rm inv}/(\Gamma_{\rm inv} + \Gamma_{\rm SM})$. In Fig. 12, we vary three parameters, (θ, $|y'/y|$, m_2), and their values are

$$\theta/\pi = 0, 0.05, 0.01, \cdots, 1.00, \tag{37}$$

$$|y'/y|^{-1} = 1, 1.5, 2.0, \cdots, 20.0, \tag{38}$$

$$m_2 = 150, 160, \cdots, 500. \tag{39}$$

Other parameters are fixed by the dark matter mass and the relic abundance. We find that a smaller spin-independent cross section gives rise to a smaller branching fraction of the Higgs invisible decay. We also find that the ILC can detect the signal of this model by searching for the Higgs invisible decay even if the XENON1T experiment does not find any dark matter signals. This is a different feature between this model and models S1 and S2. Again, by having y_S and y_P couple simultaneously, the invisible width can be large even if the spin-independent cross section is small.

C. S and T parameters

The contributions to the $\Pi_{VV'}$'s from the dark matter sector are given by

$$\Pi_{WW} = -\frac{g^2}{16\pi^2}\sum_i ((|\mathcal{C}_{L,i}|^2 + |\mathcal{C}_{R,i}|^2)H(m_i, m_D) + 4{\rm Re}(\mathcal{C}_{L,i}\mathcal{C}^*_{R,i})m_D m_i B_0(m_i, m_D)), \tag{40}$$

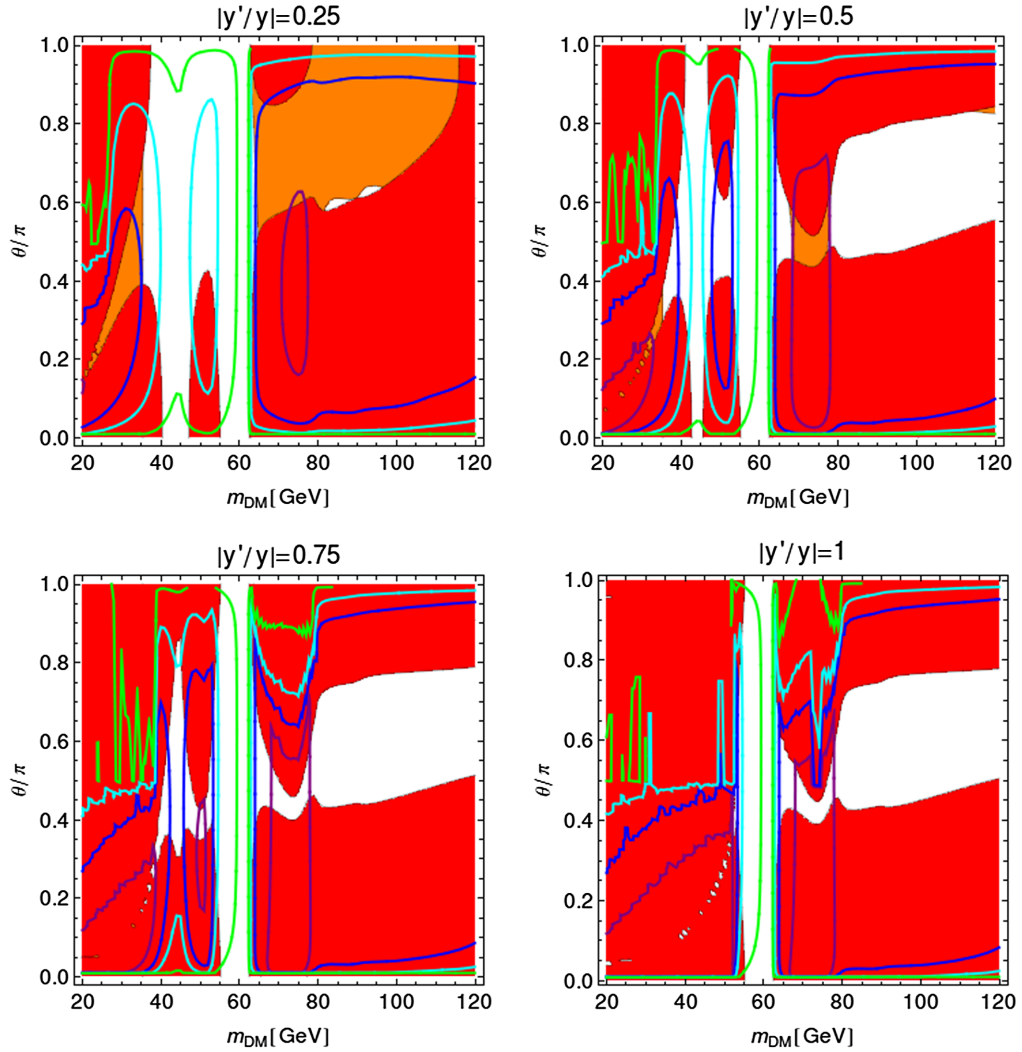

FIG. 11 (color online). The electron EDM in the $m_{\rm DM}$–θ plane. We take $|y'/y| = 0.25, 0.5, 0.75, 1$ in each panel, and $m_D = 200$ GeV in all of the panels. At each point, we set the overall size of the Yukawa couplings y and y' to realize $\Omega_{\rm DM}h^2 = 0.12$. The green, cyan, blue, and purple lines show $|d_e| = 10^{-30}, 10^{-29}, 3\times10^{-29}$, and $9\times10^{-29}e$cm, respectively. The red regions are excluded by the constraint on the spin-independent cross section from the LUX experiment [36]. The orange regions are not excluded by LUX but they are excluded by the constraint on the spin-dependent cross section from the XENON100 experiment [63].

$$\Pi_{ZZ} = -\frac{g^2}{c^2}\frac{(1-2s^2)^2}{32\pi^2}(H(m_D,m_D)+2m_D^2B_0(m_D,m_D)) - \frac{g^2}{c^2}\frac{1}{32\pi^2}\sum_{i,j}((|\mathcal{N}_{L,ij}|^2+|\mathcal{N}_{R,ij}|^2)H(m_i,m_j) + 4\mathrm{Re}(\mathcal{N}_{L,ij}\mathcal{N}_{R,ji})m_im_jB_0(m_i,m_j)), \quad (41)$$

$$\Pi_{Z\gamma} = -\frac{eg}{c}\frac{1-2s^2}{16\pi^2}(H(m_D,m_D)+2m_D^2B_0(m_D,m_D)), \quad (42)$$

$$\Pi_{\gamma\gamma} = -\frac{e^2}{8\pi^2}(H(m_D,m_D)+2m_D^2B_0(m_D,m_D)). \quad (43)$$

The definitions of B_0 and H are given in the Appendix. By using the above two-point functions, S and T are calculated using the formulas given in Eqs. (24) and (25). We show numerical results for the S and T parameters in Fig. 13.

D. Electric dipole moment

In model F12, as we have seen in Sec. II, the Yukawa couplings of the dark matter can have a CP-violating phase, and thus we can probe the dark matter sector by measuring the EDMs [14,15,67]. In this model, the two-loop diagram contributes to the EDMs and its contribution is given by[4]

[4]We have checked that our calculation is consistent with Ref. [67].

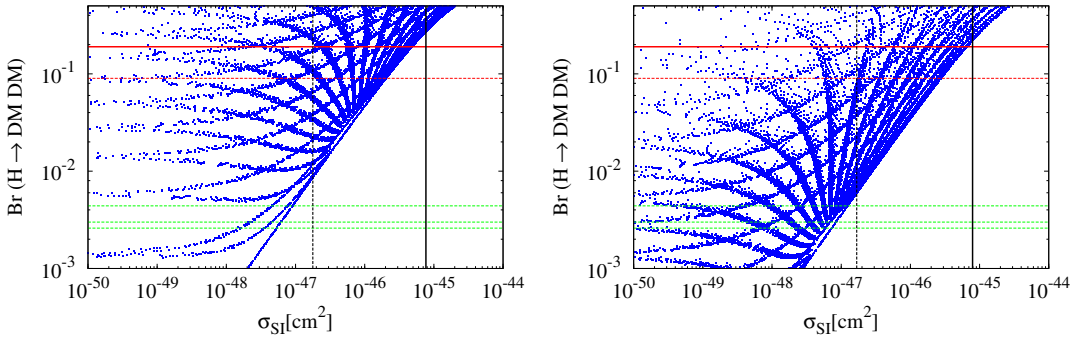

FIG. 12 (color online). The spin-independent cross section versus $\mathrm{Br}(h \to 2\mathrm{DM})$ for $m_{\mathrm{DM}} = 40$ GeV (left panel) and $m_{\mathrm{DM}} = 45$ GeV (right panel) in model F12. (See the main text for the parameters that we used.) The red solid line is the current bound [11]. The red dashed line is the future prospect at the LHC with 300 fb^{-1} [39]. The three green dashed lines are the future prospects of the ILC (250 GeV with 250 fb^{-1}, 500 GeV with 500 fb^{-1}, and 1 TeV with 1 ab^{-1} [39]). The black solid line is the current bound from the LUX experiment. The black dashed line is the future prospect of XENON1T.

$$\frac{d_f}{e} = 2T_{3f}\sum_{i=1}^{3}\left(\frac{g^2}{16\pi^2}\right)^2 \mathrm{Im}[\mathcal{C}_{L,i}\mathcal{C}^*_{R,i}]\frac{m_i m_D m_f}{m_W^4} \times \int_0^1 \frac{dx}{x}\frac{\log M_i^2(x)/m_W^2}{M_i^2(x)/m_W^2 - 1}, \tag{44}$$

where $M_i^2(x) = m_i^2/(1-x) + m_D^2/x$. In the limit $m_D \gg m_S, yv, y'v$,

$$\frac{d_f}{e} \simeq \frac{\alpha^2 T_{3f} m_f}{64\pi^2 s_W^4}\frac{\mathrm{Im}(yy')v^2 m_S}{m_W^2 m_D^3}\left(\log\frac{m_D^2}{m_W^2} + 1\right). \tag{45}$$

Numerically,

$$d_e \simeq 8.6\times 10^{-30} e\ \mathrm{cm} \times \mathrm{Im}(yy')\left(\frac{m_S}{100\ \mathrm{GeV}}\right) \times \left(\frac{m_D}{1000\ \mathrm{GeV}}\right)^{-3}\left(\log\frac{m_D^2}{m_W^2} + 1\right). \tag{46}$$

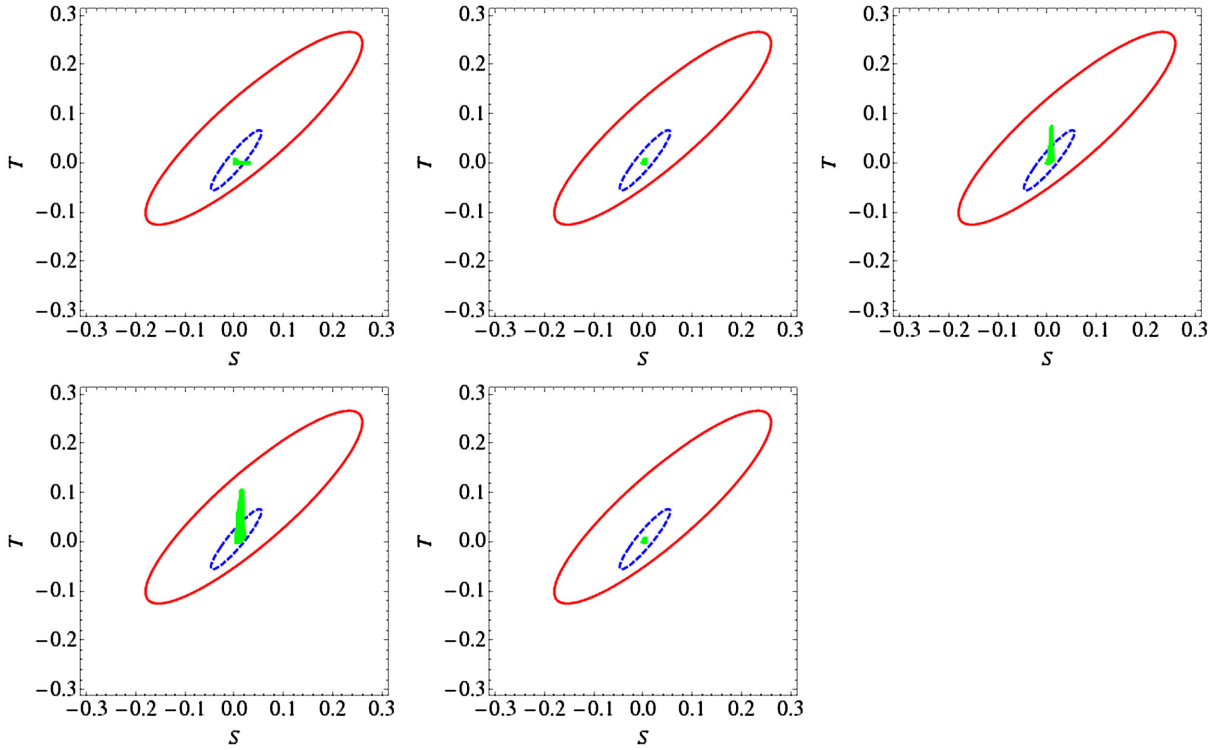

FIG. 13 (color online). The S and T parameters for $m_{\mathrm{DM}} = 40$ GeV (upper left), $m_{\mathrm{DM}} = 45$ GeV (upper middle), $m_{\mathrm{DM}} = 60$ GeV (upper right), $m_{\mathrm{DM}} = 70$ GeV (lower left), and $m_{\mathrm{DM}} = 200$ GeV (lower right). The red line is the current bound at 95% C.L. [65]. The blue dashed line is GFITTER's future prospect at the ILC [66]. The green dots are represent the current direct-search results from the LUX experiment.

The constraint on the electron EDM is given by the ACME experiment [68],

$$|d_e| < 8.7 \times 10^{-29} e \text{ cm} \quad (90\% \text{ C.L.}). \tag{47}$$

In Fig. 11, we show that the nonzero CP-violating phase opens a large parameter space in order to avoid the constraints from the direct-detection experiments. The figure shows that the electron EDM measurement is very useful for probing such a region. We show the numerical result for the electron EDM in Fig. 14, along with future prospects [69–71].

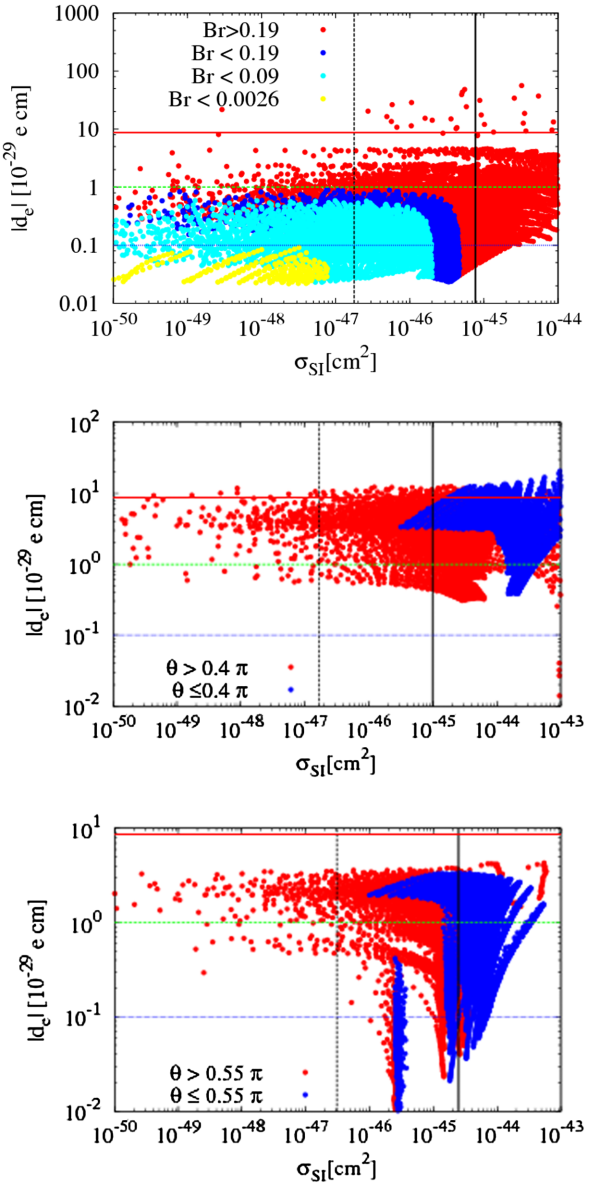

FIG. 14 (color online). The spin-independent cross section versus the electron EDM for $m_{\rm DM} = 40$ GeV (upper), 70 GeV (middle), and $m_{\rm DM} = 200$ GeV (lower). The red solid line is the current bound from the ACME experiment. The green and blue dashed lines are future prospects [69,71]. The black solid line is the current bound from the LUX experiment. The black dashed line is the future prospect of XENON1T.

In the upper panel of Fig. 14, we also show the branching fraction of the Higgs invisible decay. The red region is already excluded at the LHC [11]. The blue region is within the reach of the LHC [39]. The cyan region will be searched by the ILC experiment [39]. We find that the ILC has the capability to seek the parameter region that both dark matter direct-detection experiments and EDM experiments cannot access.

E. Direct search

In the case when $m_S, yv, y'v \ll m_D$, f^0_2, f^0_3, and $f^\pm$ approximately form an SU(2) doublet and their masses are almost degenerated. The main decay modes of heavy matter are $f^0_{2,3} \to f_1(h/Z)$ and $f^\pm \to f_1 W^\pm$. The main production channel at the LHC is $pp \to f^0_{2,3} f^\pm \to f_1 f_1 W^\pm(Z/h)$. Such channels are searched in the context of electroweakino searches in supersymmetric models. The most sensitive channels are the trilepton mode [72] and the one lepton with two b jets mode [73]. The former mode makes the constraint on $\sum_i \sigma(pp \to f^0_i f^\pm)\text{Br}(f^0_i \to f_1 Z)\text{Br}(f^\pm \to f_1 W^\pm)$, and the latter makes the constraint on $\sum_i \sigma(pp \to f^0_i f^\pm)\text{Br}(f^0_i \to f_1 h)\text{Br}(f^\pm \to f_1 W^\pm)$. We estimated the production cross section by using PROSPINO2 [74] by taking the pure Higgsino limit. In Fig. 15, we show the present status of the constraint from direct searches on model F12. Reference [75] showed that $m_{\rm wino} \lesssim 800$ GeV can be probed by the trilepton search at the 14 TeV LHC with 3000 fb^{-1} for the wino, i.e., an SU(2) triplet Majorana fermion. Since the production cross section of $f^0_{2,3} f^\pm$ in model F12 is half of the cross section for the pair production of a neutral wino and a charged wino, we expect $m_D \lesssim 600$–700 GeV can be probed at the 14 TeV LHC with 3000 fb^{-1}.

V. DISCRIMINATION OF MODELS S1 AND F12

So far we have discussed four dark matter models, which are listed in Table I. Model S2 predicts a ∼10% deviation of $\mu(h \to 2\gamma)$ from the SM, and the light mass region ($m_{\rm DM} < 72$ GeV) will be covered at the ILC. On the other hand, models S1 and F12 do not predict a deviation in the Higgs diphoton signal strength, and we can distinguish them from model S2. Model F23 predicts a deviation of $\mu(h \to 2\gamma)$ from the SM that is too large, and it is already excluded.

The difference between models S1 and F12 is very subtle because the phenomenology of dark matter in models S1 and F12 is quite similar. If direct-search experiments discover dark matter, and if the dark matter mass and its spin-independent cross section are consistent with the prediction of model S1, then we will have to discriminate model S1 from model F12 using some other combination of

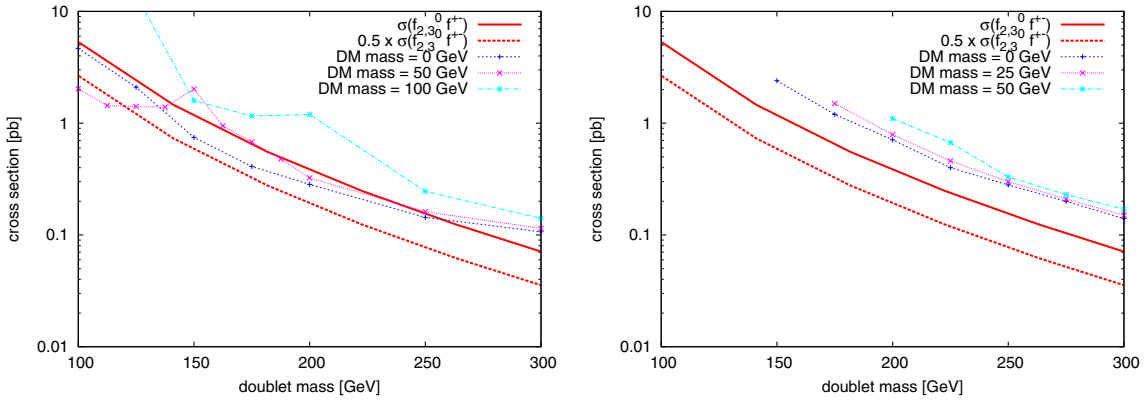

FIG. 15 (color online). Constraint on the production cross section of $f^0_{2,3}f^{\pm}$ at the $\sqrt{s} = 8$ TeV LHC. The left panel shows the trilepton search [72], and the right panel shows the search for one lepton with two b jets [73].

observables. In this section, we discuss the discrimination of models S1 and F12 for each mass region.

A. $m_{\rm DM} \lesssim 53$ GeV

In this mass region, as we can see from Fig. 9, model S1 is already excluded by the dark matter direct search, while model F12 is not. Therefore we can distinguish these two models in this mass region using the dark matter direct search.

B. 53 GeV $\lesssim m_{\rm DM} \lesssim m_h/2$

We show the correlations between the spin-independent cross section, the electron EDM, and the branching fraction of the Higgs invisible decay in Fig. 16. Here we take

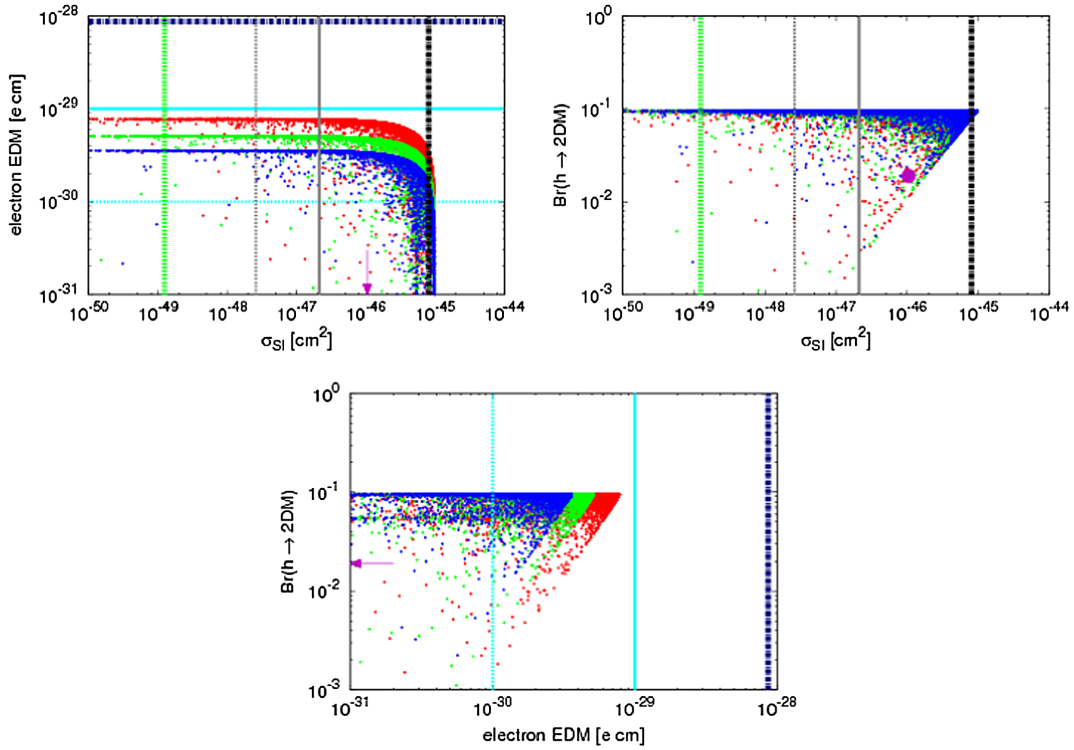

FIG. 16 (color online). Discrimination of dark matter models for $m_{\rm DM} = 55$ GeV. The red, green, and blue points show $m_D = 200, 300$, and 400 GeV, respectively. The magenta points or arrows show model S1. The black chain line is the constraint from LUX, and the gray solid and dotted lines show the future prospects of XENON1T and LZ, respectively. The experimental values are taken from Ref. [37]. The green dotted line shows the discovery limit which is caused by atmospheric and astrophysical neutrinos. The blue chain line shows the constraint from the ACME experiment. The solid turquoise line shows the future prospect of measurements of Fr atoms [69]. The dotted turquoise line shows the future prospect of measurements of the YbF molecule and WN ion [70,71].

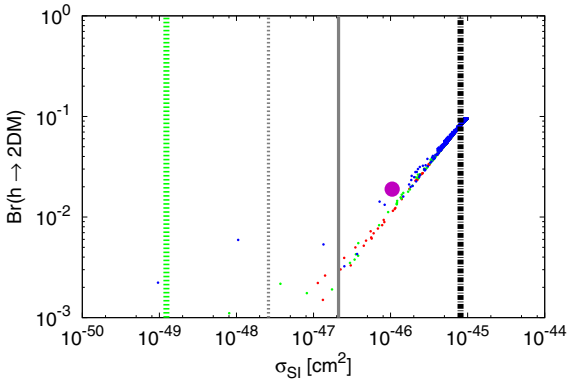

FIG. 17 (color online). Discrimination of dark matter models for $m_{\rm DM} = 55$ GeV in a parameter region with $|d_e| < 10^{-30} e$cm, i.e., in this case future experiments [70,71] cannot observe the electron EDM. The meaning of the lines and the magenta point are the same as in Fig. 16.

$m_{\rm DM} = 55$ GeV as a benchmark. In these plots, for given $m_{\rm DM}$ and m_D, we take $|y/y'| \in [0, 1]$ and $\theta \in [0, \pi]$ and take the overall size of y and y' to give $\Omega_{\rm DM}h^2 = 0.1196$. In model F12 with m_D $\mathcal{O}(100)$ GeV, this model gives various observables. Obviously, the electron EDM is a powerful tool for discrimination between models S1 and F12 because model S1 does not include a new CP violation source and does not predict any EDMs. We also show the possibility that future experiments [70,71] do not observe the electron EDM in Fig. 17. In this case, the branching fraction of the Higgs invisible decay is helpful to distinguish the two models. The model F12 predicts a wide range for the invisible width, while model S1 predicts a point.

We also check the case with $m_{\rm DM} = 60$ GeV. In this case, both the electron EDM and the branching fraction of the Higgs invisible decay are smaller than the future prospects, and we have to rely on direct searches for exotic

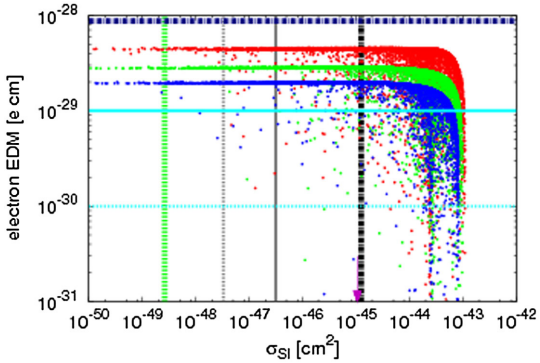

FIG. 18 (color online). Scatter plot of $\sigma_{\rm SI}$–d_e plane and $\sigma_{\rm SI}$–S plane for $m_{\rm DM} = 100$ GeV. Red, green and blue points shows $m_D = 200, 300$ and 400 GeV, respectively. Magenta points or arrows show model S1. For the explanation of black, green, blue, turquoise lines, see the caption of Fig. 16.

particles (other than dark matter particles) in model F12 in order to discriminate models S1 and F12.

C. 100 GeV $\lesssim m_{\rm DM}$

In the case with $m_{\rm DM} = 100$ GeV, we show a scatter plot in the $\sigma_{\rm SI}$–d_e and $\sigma_{\rm SI}$–S planes in Fig. 18. In these plots, for given $m_{\rm DM}$ and m_D, we take $|\lambda/\lambda'| \in [0, 1]$ and $\theta \in [0, \pi]$ and take the overall size of λ and λ' to give $\Omega_{\rm DM}h^2 = 0.1196$. Here, we can see that the electron EDM is a very useful tool for the discrimination of the models.

VI. CONCLUSION AND DISCUSSIONS

In this paper, we considered several simple dark matter models, and studied their phenomenological aspects comprehensively. In particular, we discussed the experimental prospects of each dark matter model and how to discriminate them for the case when the dark matter mass is smaller than $\mathcal{O}(100)$ GeV.

In this mass region, model S2 predicts a 10% deviation of $\mu(h \to 2\gamma)$, and thus most of the region for light dark matter in model S2 can be covered by the LHC and the ILC. Model F23 predicts a large $\mu(h \to 2\gamma)$ deviation and is already excluded. For model F12, in the case where the doublet Dirac mass m_D is a few hundred GeV, the observation of the electron EDM and the discovery of doublet fermions are expected. For 53 GeV $< m_{\rm DM} <$ $m_h/2$ and 100 GeV $< m_{\rm DM}$, if the electron EDM is not observed, it is not an easy task to distinguish models S1 and F12, because the spin-independent cross section for model F12 can mimic that for model S1 due to the existence of the blind spots. The measurements of the branching fraction of the Higgs invisible decay at the ILC provide us with useful information in this case. Of course, the direct search for other Z_2-odd particles is also useful to distinguish models S1 and F12. We summarize the features of each model for light dark matter in Table II and the current status of the dark matter mass region in Fig. 19. We also summarize how to distinguish the light dark matter models that we addressed in this paper in Fig. 20.

TABLE II. Summary of light dark matter. The cells marked "..." are not treated in this paper.

	S1	S2	F12	F23
$\mu(h \to 2\gamma)$	1 (same as SM)	∼0.9	1 (same as SM)	$\lesssim$0.8
EWPT	(same as SM)			...
EDM	(same as SM)	(same as SM)	$> 10^{-30} e$ cm is possible	...
Collider	...	...	LHC	...

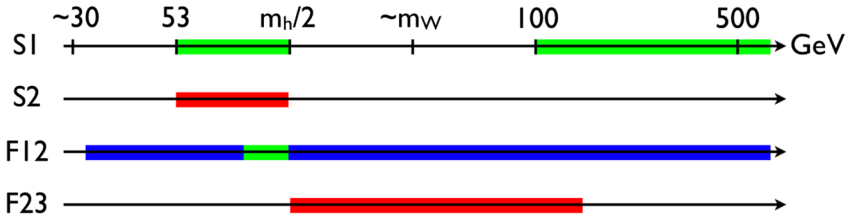

FIG. 19 (color online). Summary of the current status of each model in the light dark matter mass region. The shaded regions are consistent with the LUX experiment. The red shaded regions predict a smaller diphoton signal strength. The blue shaded regions predict the EDM.

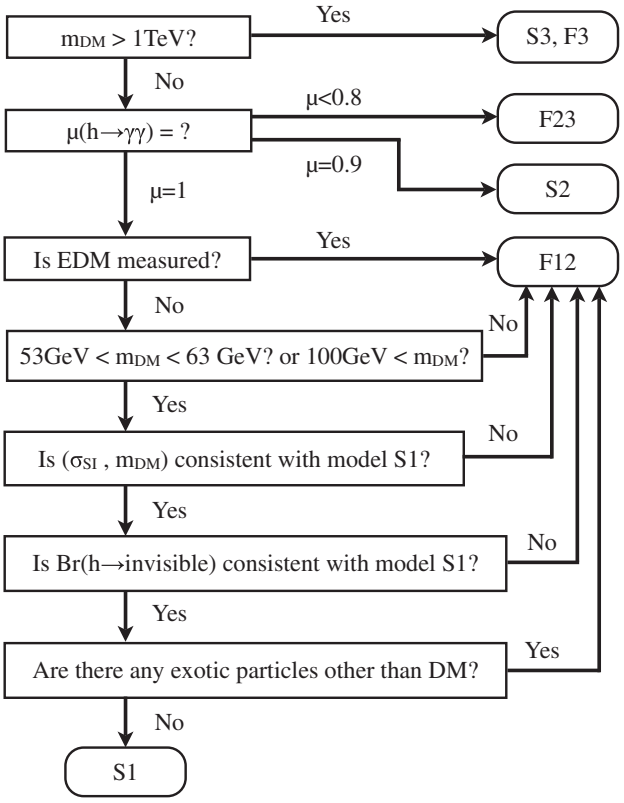

FIG. 20. Model chromatography for light dark matter models. We consider models S1, S2, S3, F12, F23, and F3. Here, we assume that only DM-sector particles give contributions to the electron EDM and the deviation of the diphoton signal strength from the SM value.

ACKNOWLEDGMENTS

This work is supported by JSPS Grant-in-Aid for Young Scientists (B) (No. 23740165 [RK]), MEXT Grant-in-Aid for Scientific Research on Innovative Areas (No. 25105011 [RK]), Grant-in-Aid for Scientific research from the Ministry of Education, Culture, Sports, Science and Technology (MEXT), Japan, (No. 23104006 [TA]), and JSPS Research Fellowships for Young Scientists [RS].

APPENDIX: LOOP FUNCTIONS

Here, we summarize the loop functions that are used in the calculation of EWPT and diphoton signal strength.

1. Loop functions for oblique corrections

The scalar loop contribution to the vector-boson two-point function is given as

$$\mu^{4-d}\left[\int\frac{d^dk}{(2\pi)^d}\frac{(2k+p)^\mu(2k+p)^\nu}{[(k+p)^2-m_1^2][k^2-m_2^2]}+\int\frac{d^dk}{(2\pi)^d}\frac{g^{\mu\nu}}{k^2-m_1^2}+\int\frac{d^dk}{(2\pi)^d}\frac{g^{\mu\nu}}{k^2-m_2^2}\right]=\frac{i}{16\pi^2}4\tilde{B}_{22}(m_1,m_2)g^{\mu\nu}+(p^\mu p^\nu\,\text{terms}). \tag{A1}$$

The fermion loop contribution to the vector-boson two-point function is given as

$$\begin{aligned}(-1)\mu^{4-d}\int\frac{d^dk}{(2\pi)^d}\int\text{tr}\Big[&\gamma^\mu(g_LP_L+g_RP_R)\\&\times\frac{\not{k}+\not{p}+m_1}{(k+p)^2-m_1^2}\gamma^\mu(h_LP_L+h_RP_R)\frac{\not{k}+m_2}{k^2-m_2^2}\Big]\\&=\frac{-i}{16\pi^2}[(g_Lh_L+g_Rh_R)H(m_1,m_2)\\&+2(g_Lh_R+g_Rh_L)m_1m_2B_0(m_1,m_2)]g^{\mu\nu}+\cdots.\end{aligned} \tag{A2}$$

Here, $\cdots$ represents terms which are proportional to $p^\mu p^\nu$. If the internal fermion is the same Majorana fermion, Eq. (A2) has a symmetric factor of $1/2$. B_0, H, and $\tilde{B}_{22}$ are loop functions given in Ref. [76], and their integral forms are

$$B_0(m_1,m_2)=\frac{1}{\hat{\epsilon}}-\int_0^1dx\log\frac{\Delta}{\mu^2}, \tag{A3}$$

$$\begin{aligned}&H(m_1,m_2)\\&=\frac{1}{\hat{\epsilon}}\left(\frac{2}{3}p^2-m_1^2-m_2^2\right)-\int_0^1dx\Big(4x(1-x)p^2\\&\quad-2(1-x)m_1^2-2xm_2^2\Big)\log\frac{\Delta}{\mu^2},\end{aligned} \tag{A4}$$

$$\begin{aligned}\tilde{B}_{22}(m_1,m_2)=&-\frac{1}{\hat{\epsilon}}\frac{p^2}{12}+\frac{1}{4}\int_0^1dx((1-2x)^2p^2\\&-(m_1^2-m_2^2)(1-2x))\log\frac{\Delta}{\mu^2},\end{aligned} \tag{A5}$$

where $\Delta = xm_1^2 + (1-x)m_2^2 - x(1-x)p^2 - i\epsilon$, $\hat{\epsilon} = 2 - d/2$ and μ is the renormalization scale in the $\overline{\rm MS}$ scheme.

2. Loop functions for the diphoton signal

The A's are loop functions, which are defined in Ref. [77]. They are defined as

$$A_1(\tau) = -\tau^{-2}(2\tau^2 + 3\tau + 3(2\tau - 1)f(\tau)), \quad \text{(A6)}$$

$$A_{1/2}^A(\tau) = 2\tau^{-1}f(\tau), \quad \text{(A7)}$$

$$A_{1/2}^H(\tau) = 2\tau^{-2}(\tau + (\tau - 1)f(\tau)), \quad \text{(A8)}$$

$$A_0(\tau) = -\tau^{-2}(\tau - f(\tau)), \quad \text{(A9)}$$

where $f(\tau)$ is defined as

$$f(\tau) = \begin{cases} \arcsin^2\sqrt{\tau} & (\tau \le 1), \\ -\frac{1}{4}\left(\log\frac{1+\sqrt{1-\tau^{-1}}}{1-\sqrt{1-\tau^{-1}}} - i\pi\right)^2 & (\tau > 1). \end{cases} \quad \text{(A10)}$$

[1] J. H. Oort, Bull. Astron. Inst. Neth. **6**, 249 (1932).
[2] F. Zwicky, Helv. Phys. Acta **6**, 110 (1933).
[3] G. Steigman and M. S. Turner, Nucl. Phys. **B253**, 375 (1985).
[4] V. Silveira and A. Zee, Phys. Lett. **161B**, 136 (1985).
[5] J. McDonald, Phys. Rev. D **50**, 3637 (1994).
[6] C. P. Burgess, M. Pospelov, and T. ter Veldhuis, Nucl. Phys. **B619**, 709 (2001).
[7] J. M. Cline, K. Kainulainen, P. Scott, and C. Weniger, Phys. Rev. D **88**, 055025 (2013).
[8] R. Barbieri, L. J. Hall, and V. S. Rychkov, Phys. Rev. D **74**, 015007 (2006).
[9] A. Arhrib, Y. L. S. Tsai, Q. Yuan, and T. C. Yuan, J. Cosmol. Astropart. Phys. 06 (2014) 030.
[10] M. Krawczyk, D. Sokolowska, and B. Swiezewska, in *Proceedings of Toyama International Workshop: "Higgs as a Probe of New Physics 2013," Toyama, Japan, 13–16 February, 2013*, http://jodo.sci.u-toyama.ac.jp/theory/HPNP2013/HPNP2013Proceedings.pdf; M. Krawczyk, D. Sokolowska, P. Swaczyna, and B. Swiezewska, J. High Energy Phys. 09 (2013) 055.
[11] G. Belanger, B. Dumont, U. Ellwanger, J. F. Gunion, and S. Kraml, Phys. Rev. D **88**, 075008 (2013).
[12] T. Araki, C. Q. Geng, and K. I. Nagao, Phys. Rev. D **83**, 075014 (2011).
[13] M. Cirelli, A. Strumia, and M. Tamburini, Nucl. Phys. **B787**, 152 (2007).
[14] R. Mahbubani and L. Senatore, Phys. Rev. D **73**, 043510 (2006).
[15] F. D'Eramo, Phys. Rev. D **76**, 083522 (2007).
[16] R. Enberg, P. J. Fox, L. J. Hall, A. Y. Papaioannou, and M. Papucci, J. High Energy Phys. 11 (2007) 014.
[17] T. Cohen, J. Kearney, A. Pierce, and D. Tucker-Smith, Phys. Rev. D **85**, 075003 (2012).
[18] C. Cheung and D. Sanford, J. Cosmol. Astropart. Phys. 02 (2014) 011.
[19] A. Dedes and D. Karamitros, Phys. Rev. D **89**, 115002 (2014).
[20] P. A. R. Ade *et al.* (Planck Collaboration), Astron. Astrophys. **571**, A16 (2014).
[21] N. G. Deshpande and E. Ma, Phys. Rev. D **18**, 2574 (1978).
[22] M. Cirelli, N. Fornengo, and A. Strumia, Nucl. Phys. **B753**, 178 (2006).
[23] L. Randall and R. Sundrum, Nucl. Phys. **B557**, 79 (1999).
[24] G. F. Giudice, M. A. Luty, H. Murayama, and R. Rattazzi, J. High Energy Phys. 12 (1998) 027.
[25] Y. G. Kim and K. Y. Lee, Phys. Rev. D **75**, 115012 (2007).
[26] A. Alloul, N. D. Christensen, C. Degrande, C. Duhr, and B. Fuks, Comput. Phys. Commun. **185**, 2250 (2014).
[27] G. Belanger, F. Boudjema, A. Pukhov, and A. Semenov, Comput. Phys. Commun. **185**, 960 (2014).
[28] G. Aad *et al.* (ATLAS Collaboration), Phys. Rev. D **90**, 052004 (2014).
[29] CMS Collaboration, Report No. CMS-PAS-HIG-14-009.
[30] M. C. Bento, O. Bertolami, and R. Rosenfeld, Phys. Lett. B **518**, 276 (2001).
[31] Y. Mambrini, Phys. Rev. D **84**, 115017 (2011); A. Djouadi, O. Lebedev, Y. Mambrini, and J. Quevillon, Phys. Lett. B **709**, 65 (2012); A. Djouadi, A. Falkowski, Y. Mambrini, and J. Quevillon, Eur. Phys. J. C **73**, 2455 (2013).
[32] X. G. He, T. Li, X. Q. Li, J. Tandean, and H. C. Tsai, Phys. Rev. D **79**, 023521 (2009).
[33] E. Ponton and L. Randall, J. High Energy Phys. 04 (2009) 080.
[34] A. Bandyopadhyay, S. Chakraborty, A. Ghosal, and D. Majumdar, J. High Energy Phys. 11 (2010) 065.
[35] W. L. Guo and Y. L. Wu, J. High Energy Phys. 10 (2010) 083.
[36] D. S. Akerib *et al.* (LUX Collaboration), Phys. Rev. Lett. **112**, 091303 (2014).
[37] J. L. Feng *et al.*, arXiv:1401.6085.
[38] J. Billard, L. Strigari, and E. Figueroa-Feliciano, Phys. Rev. D **89**, 023524 (2014).
[39] H. Baer *et al.*, arXiv:1306.6352.
[40] L. Lopez Honorez, E. Nezri, J. F. Oliver, and M. H. G. Tytgat, J. Cosmol. Astropart. Phys. 02 (2007) 028.
[41] E. M. Dolle and S. Su, Phys. Rev. D **80**, 055012 (2009).
[42] D. Sokolowska, arXiv:1107.1991.
[43] A. Goudelis, B. Herrmann, and O. Stål, J. High Energy Phys. 09 (2013) 106.
[44] A. Arhrib, Y. L. S. Tsai, Q. Yuan, and T. C. Yuan, J. Cosmol. Astropart. Phys. 06 (2014) 030.

[45] L. Lopez Honorez, E. Nezri, J. F. Oliver, and M. H. G. Tytgat, J. Cosmol. Astropart. Phys. 02 (2007) 028.
[46] M. Klasen, C. E. Yaguna, and J. D. Ruiz-Alvarez, Phys. Rev. D **87**, 075025 (2013).
[47] A. Pierce and J. Thaler, J. High Energy Phys. 08 (2007) 026.
[48] E. Lundstrom, M. Gustafsson, and J. Edsjo, Phys. Rev. D **79**, 035013 (2009).
[49] E. Dolle, X. Miao, S. Su, and B. Thomas, Phys. Rev. D **81**, 035003 (2010).
[50] X. Miao, S. Su, and B. Thomas, Phys. Rev. D **82**, 035009 (2010).
[51] B. Swiezewska, Phys. Rev. D **88**, 055027 (2013); **88**, 119903(E) (2013).
[52] A. Arhrib, R. Benbrik, and N. Gaur, Phys. Rev. D **85**, 095021 (2012).
[53] M. E. Peskin and T. Takeuchi, Phys. Rev. D **46**, 381 (1992).
[54] S. Andreas, T. Hambye, and M. H. G. Tytgat, J. Cosmol. Astropart. Phys. 10 (2008) 034.
[55] B. Swiezewska and M. Krawczyk, Phys. Rev. D **88**, 035019 (2013).
[56] M. E. Peskin, arXiv:1207.2516.
[57] A. Heister *et al.* (ALEPH Collaboration), Phys. Lett. B **533**, 223 (2002).
[58] G. Abbiendi *et al.* (OPAL Collaboration), Eur. Phys. J. C **29**, 479 (2003).
[59] J. Abdallah *et al.* (DELPHI Collaboration), Eur. Phys. J. C **34**, 145 (2004).
[60] LEP2 SUSY Working Group, http://lepsusy.web.cern.ch/lepsusy/www/inoslowdmsummer02/charginolowdm_pub.html.
[61] ATLAS Collaboration, Report No. ATLAS-CONF-2014-009.
[62] CMS Collaboration, Eur. Phys. J. C **74**, 3076 (2014).
[63] P. Beltrame (XENON Collaboration), arXiv:1305.2719.
[64] A. Djouadi, J. Kalinowski, and M. Spira, Comput. Phys. Commun. **108**, 56 (1998).
[65] J. Beringer *et al.* (Particle Data Group Collaboration), Phys. Rev. D **86**, 010001 (2012).
[66] M. Baak, J. Cúth, J. Haller, A. Hoecker, R. Kogler, K. Mönig, M. Schott, and J. Stelzer (Gfitter Group Collaboration), Eur. Phys. J. C **74**, 3046 (2014).
[67] G. F. Giudice and A. Romanino, Phys. Lett. B **634**, 307 (2006).
[68] J. Baron *et al.* (ACME Collaboration), Science **343**, 269 (2014).
[69] Y. Sakemi *et al.*, J. Phys. Conf. Ser. **302**, 012051 (2011).
[70] D. M. Kara, I. J. Smallman, J. J. Hudson, B. E. Sauer, M. R. Tarbutt, and E. A. Hinds, New J. Phys. **14**, 103051 (2012).
[71] D. Kawall, J. Phys. Conf. Ser. **295**, 012031 (2011).
[72] ATLAS Collaboration, Report No. ATLAS-CONF-2013-035.
[73] ATLAS Collaboration, Report No. ATLAS-CONF-2013-093.
[74] W. Beenakker, R. Hopker, and M. Spira, arXiv:hep-ph/9611232.
[75] ATLAS Collaboration, Report No. ATL-PHYS-PUB-2014-010.
[76] D. M. Pierce, J. A. Bagger, K. T. Matchev, and R. j. Zhang, Nucl. Phys. **B491**, 3 (1997).
[77] A. Djouadi, Phys. Rep. **457**, 1 (2008).